

CHANDRA DISCOVERY OF LUMINOUS SUPERSOFT X-RAY SOURCES IN M81

DOUGLAS A. SWARTZ¹, KAJAL K. GHOSH¹, VALERY SULEIMANOV², ALLYN F. TENNANT³,
KINWAH WU⁴

Submitted to Astrophysical Journal

ABSTRACT

A *Chandra* ACIS-S imaging observation of the nearby galaxy M81 (NGC 3031) reveals 9 luminous soft X-ray sources. The local environments, X-ray spectral properties, and X-ray light curves of the sources are presented and discussed in the context of prevailing physical models for supersoft sources. It is shown that the sample falls within expectations based on population synthesis models taken from the literature though the high observed luminosities ($L_{obs} \sim 2 \times 10^{36}$ to $\sim 3 \times 10^{38}$ erg-s⁻¹ in the 0.2–2.0 keV band) and equivalent blackbody temperatures ($T_{eff} \sim 40$ to 80 eV) place the brightest detected M81 objects at the high luminosity end of the class of supersoft sources defined by previous *ROSAT* and *Einstein* studies of nearby galaxies. This is interpreted as a natural consequence of the higher sensitivity of *Chandra* to hotter and more luminous systems. Most of the sources can be explained as canonical supersoft sources, accreting white dwarfs powered by steady surface nuclear burning, with X-ray spectra well-fit by hot white dwarf local thermodynamic equilibrium atmosphere models. An exceptionally bright source is scrutinized in greater detail as its estimated bolometric luminosity, $L_{bol} \sim 1.5 \times 10^{39}$ erg s⁻¹, greatly exceeds theoretical estimates for supersoft sources. This source may be beyond the stability limit and undergoing a phase of mass outflow under extreme conditions. Alternatively, a model in which the observed X-ray spectrum arises from an accretion disk around a blackhole of mass $\sim 1200/(\cos i)^{1/2} M_{\odot}$ (viewed at an inclination angle i) cannot be excluded.

Subject headings: binaries: symbiotic — stars: evolution — stars: atmospheres — novae — white dwarfs — X-rays: stars

1. INTRODUCTION

Luminous supersoft X-ray sources have effective blackbody temperatures of 15–80 eV and bolometric luminosities 10^{36} to 10^{38} erg s⁻¹ (Kahabka & van den Heuvel 1997). Lacking significant emission above ~ 0.5 –1 keV, supersoft sources are easily identified using even low-resolution X-ray detectors. However, only 10 Galactic objects are listed as supersoft sources in the latest compilation of Greiner (2000a) while population synthesis studies (Di Stefano & Rappaport 1994, Yungleson et al. 1996, Di Stefano & Nelson 1996) predict of order 1000 supersoft sources could be active in ordinary galaxies like our own. Local objects are therefore of limited use for supersoft source population studies. The best opportunity is to explore nearby galaxies at high galactic latitude where intervening absorption is low, all the sources are at a common distance, a single pointing can detect a large number of sources, and their spatial distribution can be measured. Indeed, surveys conducted using the *ROSAT* and *Einstein* observatories have identified 8 supersoft sources in the LMC, 4 in the SMC, and 34 in M31 (see Greiner 1996 for a detailed listing). The high sensitivity and moderate spectral resolution make the *Chandra* X-ray Observatory an ideal facility to systematically extend supersoft source population studies to other nearby galaxies. This is the rationale for the present investigation.

A 50 ks *Chandra* ACIS-S imaging observation of the

nearby galaxy M81 reveals nine supersoft source candidates identified by broadband X-ray colors (§2). Four of these sources are located within the old population of bulge stars and all but one of the remainder are coincident with M81 spiral arms. A search of known objects finds two of the bulge sources are spatially coincident with sources of enhanced [OIII] $\lambda 5007$ Å emission; consistent with nebulae photoionized by the X-ray sources. No other spatial correlations were discovered in searches of multiwavelength archival data, contemporary radio and H α images, or published source catalogues. The two brightest supersoft source candidates are visible in archival *ROSAT* PSPC or HRI X-ray images.

Detailed X-ray spectral analysis of the three brightest sources is presented in §3. Their effective temperatures, based on line-blanketed local thermodynamic equilibrium white dwarf atmospheres and blackbody model fits, span $T_{eff} \sim 50$ to 80 eV. The corresponding inferred bolometric luminosities are $L_{bol} \sim 3 \times 10^{38}$ to $\sim 1.5 \times 10^{39}$ erg s⁻¹ ranking the brightest M81 objects among the hottest and brightest of all previously-known supersoft sources. Extrapolating the spectral fits to the fainter sources implies the observed luminosities of the M81 supersoft source population range from $L_{obs} \sim 2 \times 10^{36}$ (near the sensitivity limit) to $\sim 3 \times 10^{38}$ erg-s⁻¹ in the 0.2–2.0 keV band. The brightest sources show signs of X-ray variability over the duration of the *Chandra* observation and over the approximately 10-year light curve observed by *ROSAT* (§4).

¹Universities Space Research Association, NASA Marshall Space Flight Center, SD50, Huntsville, AL, USA

²Kazan State University, Kremlevskaya str. 18, 420008 Kazan, Russia

³Space Science Department, NASA Marshall Space Flight Center, SD50, Huntsville, AL, USA

⁴MSSL, University College London, Holmbury St. Mary, Surrey, RH5 6NT, UK; and School of Physics, University of Sydney, NSW 2006, Australia

The X-ray signatures of the M81 sources are compared to well-studied objects in the (rather heterogeneous) class of supersoft sources in an effort to identify possible physical mechanisms responsible for the observed emission (§5). The brightest source cannot easily be explained by prevailing theory while the other two sources for which reliable spectral fits can be made show strong similarities to the hot close-binary accreting white dwarf (WD) systems CAL 87 and CAL 83, respectively. Some prospects for future observations are discussed (§6) and a comparison is made to the supersoft source populations observed in M31 with *ROSAT* (Supper et al. 1997, Kahabka 1999) and in M101 by *Chandra* (Pence et al. 2001).

2. OBSERVATION OF SUPERSOFT SOURCES IN M81

A 49926 second observation of a portion of the galaxy M81 was obtained with the *Chandra* Advanced CCD Imaging Spectrometer (ACIS) on 2000 May 7. The nucleus and bulge of the galaxy were located near the center of the back-illuminated S3 device of the spectroscopy array operating in imaging mode. The observation was taken in faint timed exposure mode at $3.241 \text{ s-frame}^{-1}$. The global properties of the sources detected in this data are given in Tennant et al. (2001). Standard *Chandra* X-ray Center processing has applied aspect corrections and compensated for spacecraft dither. A charge transfer inefficiency (CTI) corrector algorithm (Townesley et al. 2000)⁵ was then applied to the Level 1 event list to partially correct for the charge loss and charge smearing effects of CTI in the ACIS detectors. The data were then cleaned of bad pixels and columns. We selected the standard grade set and events in pulse invariant (PI) channels corresponding to ~ 0.1 to 8.0 keV for source detection (§ 2.1) and ~ 0.2 – 2.0 keV for spectral analysis (§ 3). The 50 ks exposure corresponds to a limiting supersoft source observed 0.2 – 2.0 keV luminosity of $\sim 2 \times 10^{36} \text{ ergs-s}^{-1}$ for a 3σ signal-to-noise ratio assuming the weak supersoft source candidates have the same spectrum as the brightest object in the class.

The detector viewing area covers 57% of the optical extent of the galaxy, defined as the ellipse of major diameter $26.9'$ corresponding to the D_{25} diameter as tabulated in de Vaucouleurs et al. (1991), oriented at position angle 157° , and with major-to-minor axis ratio 2:1 corresponding to the 60° inclination angle of M81. This area includes all of the back-illuminated (BI) S3 device, approximately half of each of the front-illuminated (FI) S2 and S4 devices, and the outer corner of the FI device I3. The data from each device is analyzed independently due to differing energy resolutions, low-energy responses, and background signals.

In addition to this primary dataset, a 2.4-ks ACIS-S image taken 2000 Mar 21 and numerous *ROSAT* PSPC and HRI datasets were used to construct long-term light curves of the brightest sources (see Immler & Wang, 2001 for details of the *ROSAT* observations).

2.1. Source Identification Criteria

X-ray sources were identified using the source detection method described in Tennant et al. (2001) that compares the data to an analytic function that approximately matches the telescope’s point-spread function (PSF) and

includes off-axis broadening. Small spatial regions centered on each source with a size encompassing the 95% encircled energy radii of the PSF (at 1.5 keV) were then selected for analysis. These regions are $< 2''$ diameter on-axis and exceed $10''$ only for sources $\gtrsim 8'$ off-axis.

Background-subtracted source counts were binned into three broad bands defined as S (0.3 – 1.0 keV), M (1.0 – 2.0 keV), and H (2.0 – 8.0 keV) and the X-ray colors $MS \equiv (M - S)/(M + S)$ and $HS \equiv (H - S)/(H + S)$ were constructed. For this purpose, two background spectra were defined for sources on S3: One for the bulge where contributions from the wings of the PSF of the bright nucleus and from a relatively high level of unresolved X-ray emission was previously detected in the data (Tennant et al. 2001) and another for the disk. Separate background spectra are defined for sources on S2 and on S4. In all cases, regions enclosing all identified sources are first excluded from the data then the spectrum of the remaining area was assigned to the background. Figure 1 shows the resulting background-corrected color-color diagram for all 81 sources detected on S3 above a signal-to-noise ratio of 3.5 (Tennant et al. 2001). The bulge and disk background spectra are also represented. Some faint sources far from the aimpoint are background-dominated. Their background-subtracted count rates in certain energy bands can be negative and the absolute values of their resulting colors may exceed unity, as seen in Figure 1.

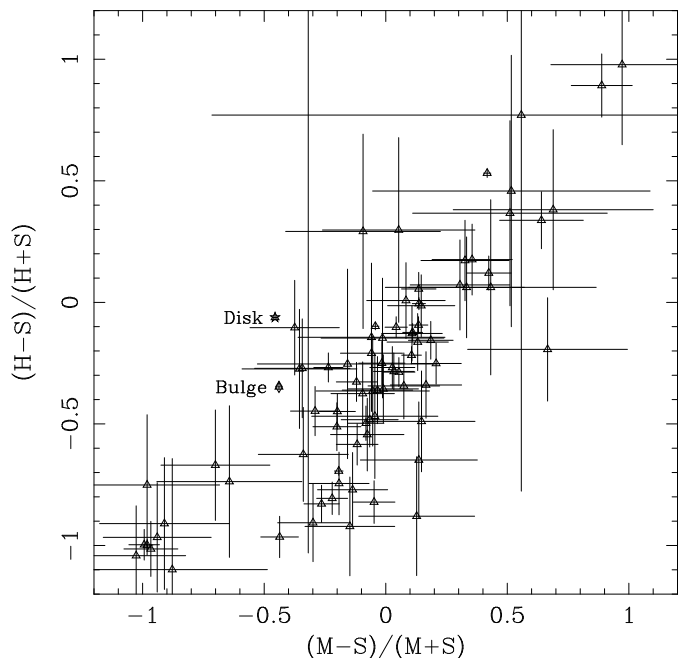


FIG. 1.— X-ray color-color diagram for M81 sources on the BI device S3. Background-subtracted source counts are binned into three bands; S (0.3 – 1.0 keV), M (1.0 – 2.0 keV), and H (2.0 – 8.0 keV). Points labeled *Disk* and *Bulge* represent the colors of the background spectra in these two regions.

Supersoft sources lie near $(-1, -1)$ in this figure (no emission above 1.0 keV). Those sources with color values ($MS < -0.5, HS < -0.5$) were tentatively classified as su-

⁵Matching response matrices were also provided by L. Townesley

persoft sources. This criteria selects 10 sources on S3, two sources on S2, and none on the remaining CCDs.

The list of sources was compared to catalogues of objects to eliminate those with properties inconsistent with supersoft sources. Supernova remnant candidate no. 17 in the catalogue of Matonick & Fesen (1997) lies within the positional uncertainty of one of the supersoft source candidates detected on S3. Though this source is weak, its spectrum appears more similar to the other X-ray sources associated with supernova remnants than to the other supersoft source candidates. Matonick & Fesen (1997) report an [OIII]/H α ratio for the supernova remnant candidate of 0.6 and an [SII]/H α ratio of 1.2. Rappaport et al. (1994) predict far different ratios, 2.4 – 6.1 and 0.1 – 0.5, respectively, for ionized regions surrounding supersoft sources. This source is therefore excluded from the list of candidate supersoft sources even though its colors ($MS = -0.88 \pm 0.39$, $HS = -1.10 \pm 0.45$) lie within our selection criteria.

Both candidate sources on S2 are coincident with bright ($m_V \sim 9$ mag) G0 stars in the PPM catalogue of stars. While they have X-ray colors (MS, HS) $\sim (-0.6, -0.8)$ they are excluded from further consideration.

The positions of the remaining candidate supersoft sources were compared to optical features in Digitized Sky Survey (DSS) and archival *Hubble*/WFPC2 images to search for potential uncatalogued foreground objects. Late-type stars with active coronae and AM Her-type magnetic cataclysmic variables (CVs) are the only foreground objects with X-ray colors falling within our selection criteria. Foreground late-type stars are easily identified in optical images as their X-ray flux is typically a small fraction of their optical flux. Am Her-type mCVs have a soft component ($T \sim 10$ – 100 eV) that may dominate any hard bremsstrahlung ($kT \sim 10$ keV) component and appear supersoft. However, their K or M star companions should be visible optically out to distances well beyond the Galactic disk in the direction of M81. It remains possible that some of the weakest supersoft source candidates could be very bright CVs, with late M-type companions, and escape optical detection provided they are located some ~ 7 kpc above the plane of the Galaxy.

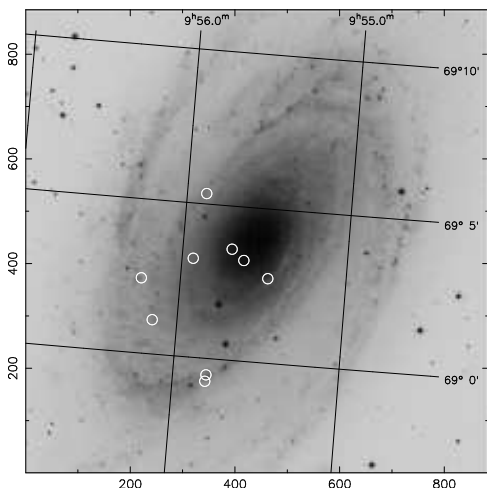


FIG. 2.— Digitized Sky Survey image of M81 with the positions of the 9 X-ray-detected supersoft source candidates superposed. Image is $\sim 15 \times 15$ arcmin. Circles have $10''$ radii.

The observed properties of the remaining 9 candidate supersoft sources, all located on the BI S3 device, are listed in Table 1 and their positions are shown superimposed on the second generation DSS image of M81 in Figure 2. Hereafter, individual supersoft sources in M81 will be referred to in order of observed brightness, column 1 of Table 1, as source N1 through source N9.

TABLE 1
OBSERVED SUPERSOFT SOURCES IN M81

No.	RA (2000)	DEC (2000)	Flux ^a	location
1	09 55 42.15	69 03 36.2	74.95	bulge
2	09 56 08.96	69 01 06.6	10.24	arm
3	09 55 53.00	69 05 20.3	3.30	arm
4	09 55 28.38	69 02 44.6	1.09	bulge
5	09 55 37.58	69 03 16.2	0.95	bulge
6	09 55 55.97	69 03 12.5	0.78	bulge
7	09 56 14.16	69 02 26.2	0.63	disk
8	09 55 47.92	68 59 28.2	0.59	arm
9	09 55 48.13	68 59 15.5	0.41	arm

^abackground-subtracted, 0.2-2.0 keV,
in units of 10^{-3} cts-s $^{-1}$

The lack of candidate supersoft sources on the FI devices is attributable to the small fraction of M81 falling within the viewing field of the FI devices, to the scarcity of X-ray sources (of all types) found far from the central regions of M81, to the weaker low energy response of the FI devices, and to the decreased off-axis source sensitivity. The detection limit for supersoft sources on the FI devices is $\sim 1.2 \times 10^{37}$ erg s $^{-1}$ or about 6 times brighter than the corresponding limit on the BI device S3.

2.2. Local Source Environments

None of the candidate supersoft sources appear extended in the *Chandra* data. As listed in Table 1, candidate sources are found throughout the bulge and disk of M81 and several lie within ~ 200 pc of spiral arms ($1' = 1.086$ kpc for the adopted distance of 3.6 Mpc to M81, Freedman et al. 1994).

While several of the candidate supersoft sources are in crowded, source-rich regions of this well-studied galaxy, only two can be unequivocally identified with catalogued objects observed at other wavelengths based on positional coincidence. These are the bulge sources N4 and N5. Three of the 4 bulge supersoft source candidates lie within the $\sim 4'$ observing field of the [OIII] $\lambda 5007$ Å survey of M81 planetary nebulae (PNe) performed by Jacoby et al. (1989). Source N4 is coincident with object ID 68 (apparent magnitude 25.33 at $\lambda 5007$ Å) and source N5 is coincident with object ID 116 (apparent magnitude 24.78) in the list of Jacoby et al. (1989). The observed X-ray luminosities of these sources exceeds that of typical planetary nebulae (10^{30} to 10^{32} erg s $^{-1}$) by several orders of magnitude assuming they are at the distance of M81. The one known exception is 1E0056.8-7154, a supersoft source associated with the Small Magellanic Cloud PNe N67 (Wang 1991) with a bolometric luminosity 2×10^{37} erg s $^{-1}$ (Heise, van Teeseling, & Kahabka 1994). The lack of detectable emission at other wavelengths, particularly in *Hubble*/WFPC2 images, indicates they are not foreground

objects lying, by chance, along the line of sight. Instead, the [OIII] $\lambda 5007$ Å emission could come from regions ionized by the X-ray source in a way similar to that observed in the LMC supersoft source CAL 83 (Remillard, Rappaport, & Macri 1995). The flux observed by Jacoby et al. (1989) is consistent with the supersoft source ionization model predictions of Rappaport et al. (1994). This is discussed in more detail in §5.2.4.

There are no point-like objects observed at other wavelengths spatially coincident with any of the remaining supersoft source candidates in M81. It is noteworthy that the exceptionally X-ray bright source N1 is within the field observed by Jacoby et al. (1989), and the recent survey of Magini et al. 2001, but is not seen at [OIII] $\lambda 5007$ Å. This source lies in a featureless region of the bulge dominated in optical bands by a high density of unresolved bulge stars. There is no nearby object discernable in archival *Hubble*/WFPC2 images of the region, nor in UV images centered at $\lambda 2490$ Å and $\lambda 1520$ Å (Hill et al. 1992), a recent (2001 May 21; A. Shafter, private communication) CCD image taken through a 70Å wide H α filter, the continuum-subtracted H α data of Devereux et al. (1995), the $\lambda 6$ and $\lambda 20$ cm radio continuum observations reported by Kaufman et al. (1996), or recent $\lambda 6$ cm data (T. Pannuti 2001, private communication).

3. X-RAY SPECTRAL ANALYSIS

The spectra of all 9 candidate sources are shown in Figure 3. They typically show a rise from low energies to a peak at ~ 0.45 to ~ 0.7 keV followed by a rapid decline toward higher energies. The shape of the low-energy portion of the spectra is determined by a combination of extinction and a decreasing ACIS detection efficiency at low energies. Above the peak, the shape is determined by a roughly exponential decline of the intrinsic source spectra.

In spectra such as these, the inferred bolometric luminosity is much higher than that observed with the peak of the intrinsic spectral energy distribution occurring at energies lower than observed. The inferred luminosities are very sensitive to the model parameters and to calibration uncertainties in the low-energy response of the BI devices. Though there is often significant flux below 0.2 keV, data at energies below this value were excluded from the fitting because of these uncertainties.

A sufficient number of counts for spectral analysis were accumulated from only the three brightest sources listed in Table 1. The spatial regions selected for spectral analysis were chosen centered on each source as described above (§2.1). Accompanying background spectra were extracted for each source from annular regions centered on the source with inner and outer radii of 30 and 50 pixels, respectively, and containing of order 200 counts. Note this procedure differs from the large background regions selected for constructing the broadband colors described previously. The procedure used in this section more accurately represents local variations in background. Spectra have been grouped into spectral bins containing a minimum of 20 counts and fitted using the XSPEC spectral fitting package (Arnaud 1996) to blackbody and to model atmosphere spectra of hot white dwarfs calculated in the local thermodynamic equilibrium (LTE) approximation.

The X-ray emission from supersoft sources is believed

to originate from nuclear burning on the surface of a WD star. The nuclear burning takes place at high optical depth within a geometrically thin, high density atmosphere with the resulting emergent spectrum highly modified by the cooler outer layers. Under these conditions, hot WD LTE model atmosphere spectra is a more appropriate approximation than is a simple blackbody assumption. Therefore, we developed tables of plane-parallel LTE model atmospheres as an alternative model for spectral fitting. Under certain circumstances the WD atmosphere may become extended or even partially ejected as a result of rapid nuclear burning. Spectra of extended, expanding, spherical atmospheres tend to be flatter than that from plane-parallel hydrostatic atmospheres with the same color temperature at maximum flux. Model atmospheres including an optically thick wind are currently in preparation.

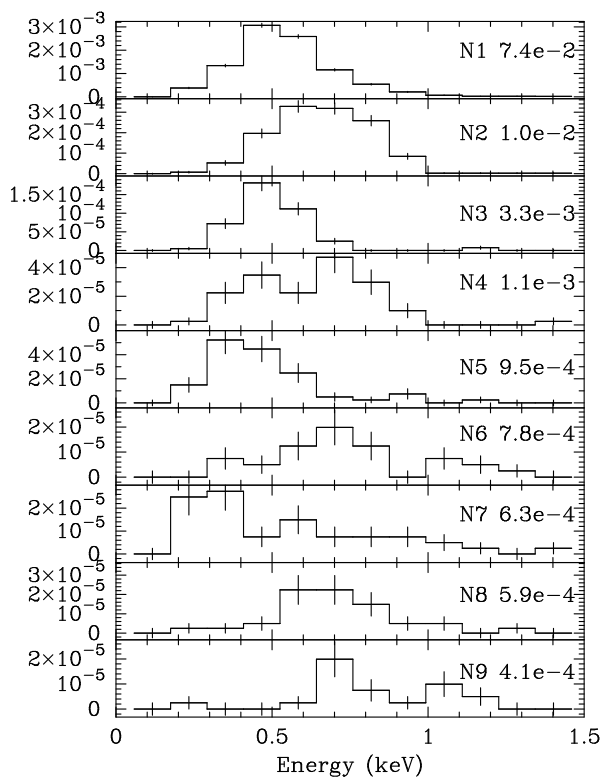


FIG. 3.— Spectra of nine supersoft source candidates. Labels denote source number and count rates over the 0.2–2.0 keV *Chandra* energy band (Table 1). Data have been binned by 8 PI channels (~ 117 eV). Vertical axis units are counts/sec.

The fundamental parameters of our plane-parallel LTE model atmospheres are the effective temperature, T_{eff} , surface gravity, g , and luminosity scale factor $K = L/(4\pi\sigma T_{eff}^4 D^2)$ where L is the bolometric luminosity, σ is the Stefan-Boltzmann constant, and D is the distance from the source to the observer. The model atmospheres were constructed following standard temperature-correction procedures as outlined in Mihalas (1978) in order to satisfy the hydrostatic and radiative equilibrium constraints. The 15 most abundant elements from H through Ni are included with bound-free opacities computed from the photoionization cross sections of Verner et al. (1993,1995). Line blanketing is included using ~ 1200

of the strongest spectral lines from the CHIANTI (v.3.0) atomic database (Dere et al. 1997).

A series of LTE model atmosphere spectra were constructed in this fashion spanning the range of parameters $10^5 \leq T_{eff} \leq 1.3 \times 10^6$ and $7.5 \leq \log(g) \leq 9.5$, as appropriate for WD atmospheres, with the scale factor K used as the model normalization in XSPEC. Tables of these models were used in conjunction with a photoelectric absorption component in fitting to the observed spectra. A separate table was constructed for each of two values of photospheric metal abundances, $Z/Z_{\odot} = 1$ and $Z/Z_{\odot} = 0.01$, relative to the solar composition given by Anders & Grevesse (1989). The lower metal abundance is roughly compatible with the observed M81 metallicities (~ 0.03) recently reported by Kong et al. (2000). In addition, a He-rich model consisting of $Z/Z_{\odot} = 0.03$ metals and 99% He by weight was also constructed.

For reference, computed hot WD LTE model atmosphere spectra at several temperatures are shown in Figure 4. Many of the edges seen in these spectra will prove key diagnostics of the properties of the candidate supersoft sources.

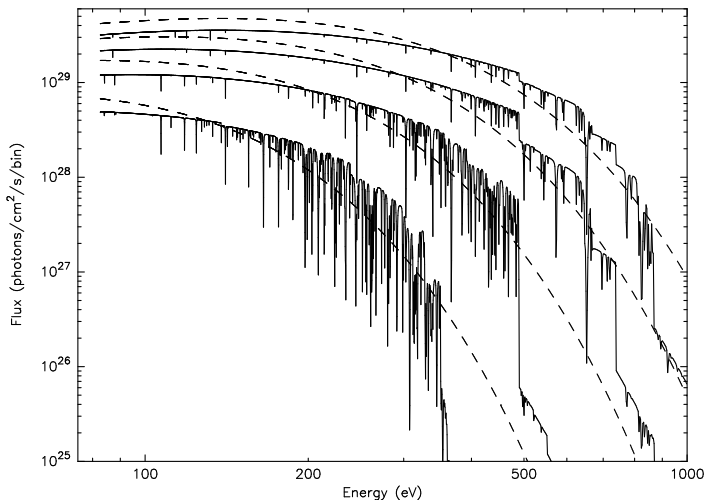


FIG. 4.— Hot white dwarf LTE atmosphere model spectra (*solid*) and corresponding blackbody spectra (*dash*) at four effective temperatures and a solar abundance composition. From top to bottom, the temperatures are $T_{eff}/10^5\text{K} = 10, 8, 6,$ and 4 . The surface gravity is $\log(g)=9$ except for the hottest model where $\log(g)=9.5$ to avoid exceeding the Eddington limit luminosity. Prominent bound-free edges are apparent at 490 eV (C VI), 670 eV (N VII), 740 eV (O VII), and 870 eV (O VIII).

3.1. Source N1

The spectral fit results for the brightest supersoft source candidate, source N1, are listed in Table 2. This and subsequent tables for the other bright sources include one column for each model. Rows list the χ^2 fit statistic, the fitted model parameters N_H (hydrogen column density), T_{eff} (blackbody or effective temperature), $\log(g)$ (surface gravity), E_{edge} (absorption edge energy) and the accompanying τ (edge optical depth). All models include photoelectric absorption from a solar abundance column. In the case of model *zvarabs*, the abundance of C and O in the absorbing column are allowed to vary. The table lists the enhancement of these elements relative to the solar values. Also listed are the observed luminosity, L_{obs} , in the 0.2–2.0 keV band, the unabsorbed luminosity, L_X , in the same

band and the bolometric luminosity, L_{bol} , as scaled from the model normalizations assuming a distance of 3.6 Mpc to M81.

The observed spectrum, best-fit absorbed blackbody model with added absorption edge at 0.26 keV (second model of Table 2), and fit residuals for source N1 are shown in Figure 5. A simple blackbody model is statistically superior to either of the LTE WD atmosphere models because of the lack of absorption edges in the observed spectrum. However, there is a feature in the blackbody fit residuals near 0.3 keV. This feature can be modelled as an edge at 0.26 ± 0.01 keV (second column of Table 2) which is very close to the neutral C K-edge at 0.277 keV. Since there is no reason to expect the galactic absorbing column to have exactly solar abundances, we also tried a variable abundance model. If a small "redshift" ($z=0.04$) is applied, this model also provided an excellent fit to the data as shown by the third column in Table 2. It is worth noting that the ACIS energy scale is uncertain at the lowest energies and thus the feature is likely a Carbon edge and the "redshift" is due to this uncertainty. As the ACIS response is also uncertain at these energies we cannot determine whether the excess Carbon is intrinsic to the source in M81, lies within our galaxy, or is a detector effect.

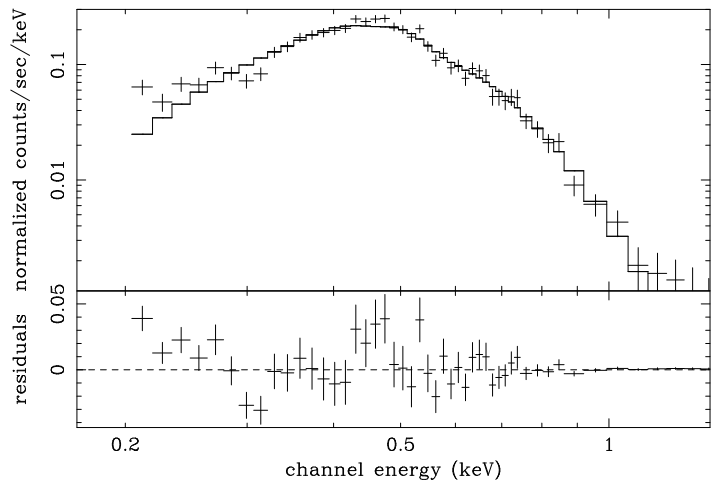


FIG. 5.— *Upper panel*: Observed spectrum of source N1 (symbols) and best-fit blackbody model with solar-abundance photoelectric absorption and added absorption edge at 0.26 keV (solid line). *Lower panel*: Fit residuals.

LTE models with an additional Raymond-Smith thermal emission component are an improvement over the single LTE component models because this added thermal component tends to fill the ~ 0.7 – 1.0 keV region of the model spectrum underestimated due to the presence of absorption edges in the LTE component. While the physical basis for such a thermal component has precedence in modeling of, *e.g.*, the recurrent nova U Sco (Kahabka et al. 1999) and the symbiotic nova SMC 3 (Jordan et al. 1996), and there is reason to believe source N1 may be near a state of dynamical outflow (see discussion in §5), the fact that a simple blackbody model provides an equally-acceptable fit allows one to conclude that the thermal component is not necessary. It should be noted that $\sim 2\%$ of the incident flux at 0.5 keV is piled up in the spectrum of source N1

TABLE 2
MODEL FITS FOR SOURCE N1

Model ^a	blackbody	blackbody + edge	blackbody w/ zvarabs ^b	LTE $Z = Z_{\odot}$	LTE $Z = 0.01Z_{\odot}$	LTE + ray $Z = Z_{\odot}$	diskbb
χ^2/dof	1.40/47	0.98/45	1.05/44	2.75/46	3.55/47	1.24/44	1.61/47
$N_H/10^{20} \text{ cm}^{-2}$	$5.7^{+0.7}_{-0.6}$	$4.2^{+1.0}_{-1.3}$	$6.3^{+0.5}_{-0.5}$	$4.2^{+0.6}_{-0.4}$	$4.0^{+0.6}_{-0.4}$	$4.4^{+0.5}_{-0.6}$	$7.4^{+0.8}_{-0.8}$
$T_{eff} \text{ eV}$	86^{+2}_{-3}	81^{+3}_{-2}	78^{+3}_{-3}	69^{+1}_{-1}	64^{+2}_{-1}	66^{+1}_{-1}	100^{+4}_{-3}
$E_{edge} \text{ keV}, \tau$	—	$0.26^{+0.02}_{-0.02}, 1.6$	—	—	—	—	—
C,O enhancement	—	—	$6.6^{+1.7}_{-1.7}, 1.5^{0.9}_{2.1}$	—	—	—	—
$\log(g) \text{ cm}^2 \text{ s}^{-1}$	—	—	—	$8.7^{+0.04}_{-0.04}$	$8.8^{+0.05}_{-0.03}$	$8.5^{+0.03}_{-0.1}$	—
thermal $kT, f(L_X)^c$	—	—	—	—	—	$0.35^{+0.12}_{0.07}, 0.18$	—
$L_{obs}/10^{38} \text{ erg s}^{-1}$	$3.0^{+0.02}_{-0.02}$	$3.0^{+0.04}_{-0.04}$	$2.9^{+0.02}_{-0.03}$	$2.9^{+0.02}_{-0.02}$	$2.9^{+0.04}_{-0.04}$	$3.0^{+0.01}_{-0.01}$	$3.0^{+0.03}_{-0.03}$
$L_X/10^{38} \text{ erg s}^{-1}$	$8.7^{+1.6}_{-1.2}$	$7.3^{+2.9}_{-1.7}$	$8.8^{+1.4}_{-1.4}$	$6.3^{+1.4}_{-1.4}$	$6.2^{+1.6}_{-1.6}$	$6.7^{+0.6}_{-0.6}$	$13.4^{+3.0}_{-2.9}$
$L_{bol}/10^{38} \text{ erg s}^{-1}$	$12.0^{+2.0}_{-2.1}$	$15.0^{+5.2}_{-1.1}$	$23.0^{+11.2}_{-8.0}$	$9.0^{+2.0}_{-1.1}$	$8.0^{+1.3}_{-1.1}$	$9.0^{+2.4}_{-2.1}$	$11.0^{+1.4}_{-1.0}/\cos i$

^aAll models include solar abundance absorption column

^bvariable-abundance absorption column with best-fit redshift $z = 0.04$

^cRaymond-Smith model temperature (keV) and fraction of L_X due to this component

resulting in detected events near 1 keV. The observed flux at 1.0–1.1 keV is 3.5% of that in the 0.5–0.55 keV band. Thus some 60% of the observed flux at 1.0–1.1 keV is due to pileup.

He-rich LTE model atmospheres were also fitted to this spectrum but no statistically-acceptable fits were obtained and they are omitted from Table 2 for brevity. The larger He opacity near the HeII edge in these models leads to a slightly lower temperature and a slightly steeper temperature gradient in spectrum-forming ($0.1 \lesssim \tau_R \lesssim 1$, where τ_R is the Rosseland mean opacity) regions of the atmosphere. The emergent flux therefore decreases near the HeII edge (due to lower temperatures) and increases slightly at the peak of the spectral energy distribution (due to the steeper gradient). The overall effect in the *Chandra* observable energy band is to produce a steeper spectrum than the H-rich LTE models. The spectrum is further steepened by the bound-free edges from intermediate-mass metals resulting in a poorer model of the data.

The blackbody shape of the observed spectrum of source N1 is reminiscent of that expected from a geometrically thin optically thick accretion disk surrounding a black hole (Shakura & Sunyaev 1973). For completeness, therefore, an accretion disk emission model was also fitted to the observations. This model accumulates the spectrum from an optically thick accretion disk observed at inclination angle i from a superposition of blackbody spectra from concentric annular elements representing the radial dependence of the disk temperature profile (Mitsuda et al. 1984, Makishima et al. 1986). The model parameters (model *diskbb*, Table 2) are the normalization, proportional to the innermost disk radius, R_{in} , for a known inclination angle and distance to the source, and the temperature at R_{in} . Assuming R_{in} corresponds to the last stable Keplerian orbit (Makishima et al. 2000) implies a mass for the central object. The best-fit normalization for source N1 corresponds to a black hole mass $M_{BH} \sim 1200/(\cos i)^{-1/2}$ assuming the last stable orbit is at 3 Schwarzschild radii. The best-fit temperature at R_{in} , $T_{in} \sim 100 \text{ eV}$, implies a bolometric luminosity $L_{bol} \sim 10^{39} \text{ erg s}^{-1}$. Not surprisingly, the color temperature T_{in} is slightly higher than that obtained from the blackbody models. The shape of the blackbody disk model is a power law of photon index

$-2/3$ at low photon energies steepening to the Wien portion of a blackbody of temperature $T_{bb} = 0.7T_{in}$ at higher energies (Makishima et al. 1986). Thus the combination of an innermost disk radius temperature slightly higher than the blackbody model temperature and a higher absorption column density is just what is needed to make the disk blackbody model mimic a standard blackbody spectrum. This is especially true in view of the fact that only the steep Wien portion of the spectrum lies within the *Chandra* energy band for low values of T_{in} and the power law portion of the blackbody disk model spectrum lies entirely below the low-energy instrumental cutoff. The lack of detectable emission at longer wavelengths at the position of source N1 (§2.2) and the lack of an observable hard power-law tail argues against the blackbody disk model.

The luminosity of source N1 is exceptionally high. The observed 0.2–2.0 keV luminosity, $L_{obs} \sim 3 \times 10^{38} \text{ erg s}^{-1}$, is slightly above the Eddington limit for a 1.4 M_{\odot} H-accreting star. The unabsorbed luminosity on the same energy range and the inferred bolometric luminosities are much higher though with high uncertainties. In contrast, L_{obs} is tightly constrained and its value does not vary among the models (Table 2). Another source of uncertainty, independent of model fit uncertainties, is the gain behavior in the BI device at low photon energies and at the -120°C focal plane temperature in use at the time of observation. Very nearly 1/3 of the observed flux from source N1 falls in the 0.2–0.4 keV energy band. A 20% uncertainty in the flux below 0.4 keV corresponds, therefore, to an additional 7% uncertainty in L_{obs} . Conservatively, then, the estimated bolometric luminosity of source N1 is at least several times $10^{38} \text{ erg s}^{-1}$ and, depending on the model, may be as high as a few $10^{39} \text{ erg s}^{-1}$. This result places severe constraints on physical models for this source (§5).

It is notable that the large range of L_X and L_{bol} is not obviously reflected in a large range of the model fit parameters N_H and T_{eff} . From Table 2, the range of these parameters among the various models (excluding *diskbb*) are $N_H = 4.9 \pm 2.0 \times 10^{20} \text{ cm}^{-2}$ and $T_{eff} = 75 \pm 11 \text{ eV}$. This substantiates the previous conjecture that the inferred luminosities are very sensitive to small variations in the model parameters. However, the differences in shape of

the blackbody and LTE model atmosphere spectra do not give systematically large differences in the derived temperatures, column densities, and luminosities as is often reported for supersoft sources.

The hot WD LTE model parameter $\log(g)$ is directly related to the mass of the assumed white dwarf. The resulting white dwarf mass is estimated to be 0.9 to 1.1 M_{\odot} for source N1.

3.2. Source N2

The spectral fit results for source N2 are listed in Table 3. The observed spectrum, best-fit LTE atmosphere model, and fit residuals are shown in Figure 6.

TABLE 3
BLACKBODY MODEL FITS FOR SOURCE N2

Model ^a	blackbody	blackbody with edge
χ^2/dof	1.87/16	0.93/14
$N_H/10^{20} \text{ cm}^{-2}$	$19.8^{+8.0}_{-7.5}$	$9.3^{+5.2}_{-5.7}$
$T_{eff} \text{ eV}$	98^{+15}_{-11}	171^{+60}_{-29}
$E_{edge} \text{ keV}, \tau$	—	$0.85^{+0.01}_{-0.03}, 3.8$
$L_{obs}/10^{38} \text{ erg s}^{-1}$	$0.4^{+0.02}_{-0.02}$	$0.5^{+0.04}_{-0.04}$
$L_X/10^{38} \text{ erg s}^{-1}$	$3.2^{+5.9}_{-2.1}$	$0.9^{+1.4}_{-0.3}$
$L_{bol}/10^{38} \text{ erg s}^{-1}$	$4.0^{+4.9}_{-0.5}$	$1.3^{+0.7}_{-0.3}$

LTE ATMOSPHERE MODEL FITS FOR SOURCE N2

Model ^a	$Z = Z_{\odot}$	$Z = 0.01Z_{\odot}$
χ^2/dof	1.38/15	1.00/15
$N_H/10^{20} \text{ cm}^{-2}$	$25.0^{+7.1}_{-8.4}$	$15.8^{+3.8}_{-4.2}$
$T_{eff} \text{ eV}$	69^{+4}_{-1}	67^{+2}_{-1}
$\log(g) \text{ cm}^2 \text{ s}^{-1}$	$8.49^{+0.03}_{-0.03}$	$8.24^{+0.40}_{-0.08}$
$L_{obs}/10^{38} \text{ erg s}^{-1}$	$0.3^{+0.01}_{-0.01}$	$0.4^{+0.03}_{-0.03}$
$L_X/10^{38} \text{ erg s}^{-1}$	$4.5^{+1.4}_{-3.7}$	$2.0^{+1.5}_{-0.8}$
$L_{bol}/10^{38} \text{ erg s}^{-1}$	$6.4^{+3.9}_{-1.3}$	$5.3^{+4.8}_{-2.1}$

^aAll models include solar abundance absorption column

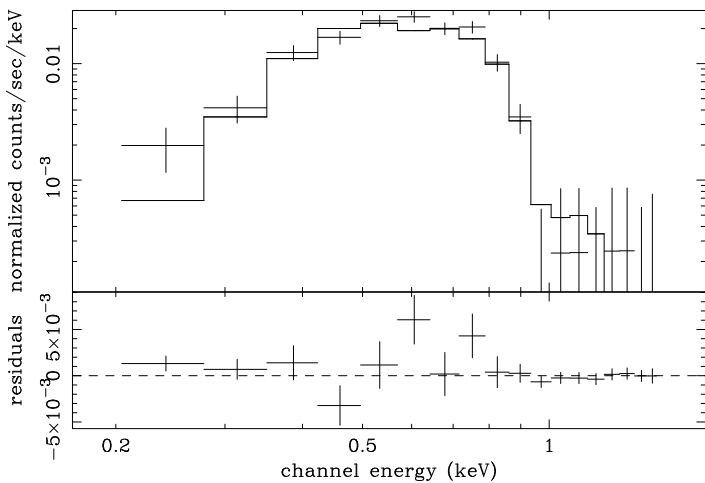


FIG. 6.— *Upper panel*: Observed spectrum of source N2 (symbols), best-fit LTE WD model atmosphere spectrum with 1% solar abundance metals and solar-abundance photoelectric absorption (solid line). *Lower panel*: Fit residuals.

In contrast to source N1, a blackbody model is clearly a poor fit to the data. A blackbody with an added absorption edge at $0.85^{+0.01}_{-0.03}$ keV gives a better fit suggesting

the presence of highly-ionized O in a very hot atmosphere. The LTE models provide significant improvements over the blackbody model. The results are not very sensitive to the assumed metal abundances though the 1% solar metal abundance model provides an improved fit. At the derived temperatures, $T_{eff} \sim 67\text{--}69$ eV, the hot WD LTE models produce numerous absorption edges. When convolved with the instrument response, the most prominent edges are those from highly ionized O at 740 eV (O VII) and 870 eV (O VIII). In the low-abundance model, the edges are not as deep and an additional Ne IX edge (1196 eV) appears in the model but is statistically insignificant in the fit.

The observed 0.2–2.0 keV luminosity derived from the hot WD LTE model atmosphere spectrum is much less than the Eddington limit for a hydrogen-accreting WD. The inferred range of bolometric luminosities exceed this limit by a factor of 2 to 3. The white dwarf mass inferred from the LTE models is 0.7 to 0.9 M_{\odot} .

3.3. Source N3

The spectral fit results for source N3 are listed in Table 4. The observed spectrum, best-fit hot WD LTE model atmosphere spectrum, and fit residuals are shown in Figure 7.

TABLE 4
MODEL FITS FOR SOURCE N3

Model ^a	blackbody	$Z = Z_{\odot}$	$Z = 0.01Z_{\odot}$
χ^2/dof	0.94/4	0.90/3	1.4/3
$N_H/10^{20} \text{ cm}^{-2}$	$10.7^{+12.6}_{-7.1}$	$4.7^{+5.3}_{-3.2}$	$8.7^{+5.4}_{-4.3}$
$T_{eff} \text{ eV}$	52^{+13}_{-5}	52^{+1}_{-1}	45^{+9}_{-6}
$\log(g) \text{ cm}^2 \text{ s}^{-1}$	—	$7.9^{+0.9}_{-0.1}$	$9.2^{+0.2}_{-1.6}$
$L_{obs}/10^{38} \text{ erg s}^{-1}$	$0.1^{+0.03}_{-0.03}$	$0.1^{+0.02}_{-0.02}$	$0.1^{+0.03}_{-0.02}$
$L_X/10^{38} \text{ erg s}^{-1}$	$2.0^{+4.5}_{-1.3}$	$0.4^{+0.3}_{-0.2}$	$1.0^{+1.9}_{-0.9}$
$L_{bol}/10^{38} \text{ erg s}^{-1}$	$4.6^{+15.3}_{-3.4}$	$1.2^{+1.3}_{-0.7}$	$1.8^{+8.0}_{-1.2}$

^aAll models include solar abundance absorption column

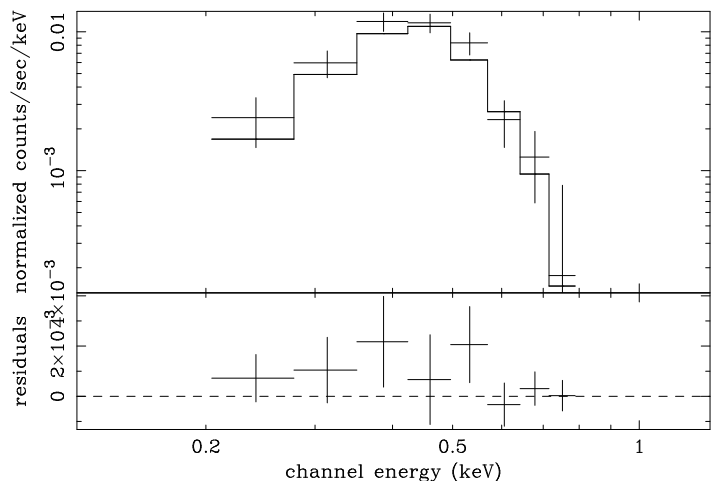


FIG. 7.— *Upper panel*: Observed spectrum of source N3 (symbols), best-fit hot WD LTE model atmosphere spectrum with solar abundance metals and solar-abundance photoelectric absorption (solid line). Spectrum and model have been rebinned to show structure. *Lower panel*: Fit residuals.

Unlike the stronger sources, the spectrum of source N3 is fit equally well by all three models and there is no spectral feature to meaningfully discriminate between models. In particular, the lack of flux above ~ 0.7 keV means that the dominant absorption edges present in the LTE atmosphere models are the relatively weak edges at C VI (490 eV) and N VII (670 eV). In this case, a slightly more absorbed blackbody model relative to the LTE models adequately mimics the observed steep decline above ~ 0.5 keV.

The observed 0.2–2.0 keV luminosity, L_{obs} , is less than the Eddington limit for a hydrogen-accreting WD and L_{bol} is comparable to the Eddington limit though, again, it is highly uncertain. The white dwarf mass inferred from the WD atmosphere LTE models is $\sim 0.5 M_{\odot}$ for the solar abundance model and is effectively unconstrained by the 1% solar metallicity model.

3.4. Other Sources

Statistically constrained model fits to the remaining sources could not be achieved. The observed count rates and similarities to the spectra of the brighter sources allow a crude extrapolation of the derived luminosities of the brighter sources to the remaining sources by the following reasoning: The ratio $L_{bol}/L_{obs} \sim 5$ for source N1 and ~ 10 –20 for sources N2 and N3. The latter two sources are associated with spiral arms. They have higher absorbing columns than source N1 which accounts for the higher L_{bol}/L_{obs} ratio. An estimate of L_{bol} can be made by assuming the ratio $L_{bol}/L_{obs} = 15$ for sources on the spiral arms and $= 5$ otherwise and noting that L_{obs} is proportional to the observed count rate (Table 1). Applying this approximation to the remaining sources using the data from Table 1 gives the following values of L_{bol} in units of 10^{37} erg s^{-1} : 2.2 (N4), 1.9 (N5), 1.6 (N6), 1.3 (N7), 3.6 (N8), and 2.4 (N9). The uncertainties in these estimates are at least a factor of three since the actual absorbing columns are unknown. This uncertainty is, alas, comparable to some of the uncertainties in L_{bol} obtained for the brightest sources.

Alternatively, luminosities can be estimated from the count rate and assuming a (blackbody) temperature and a column density. The weakest supersoft source detected has an observed luminosity of 2×10^{36} erg s^{-1} assuming an 80 eV blackbody spectrum and a column of $N_H = 8 \times 10^{20}$ cm^{-2} . This corresponds to $L_{bol} \sim 1.3 \times 10^{37}$ erg s^{-1} . L_{bol} increases to 5.2×10^{37} erg s^{-1} if the assumed temperature is lowered to 50 eV.

Temperatures cannot be so easily estimated but they are most probably of order 40–50 eV as higher temperature sources are expected to be rare based on theoretical models of supersoft sources (see §5) and cooler sources are difficult to detect with *Chandra*-ACIS. Even an intrinsically bright ($L_{bol} = 10^{38}$ erg s^{-1}) blackbody source with $T_{eff} = 25$ eV and moderate absorbing column (2 times Galactic) produces only 24 counts in the BI device and would be undetectable in the FI chips.

4. X-RAY TIMING ANALYSIS

4.1. Short-Term Variability

The 50 ks *Chandra* light curves of the brightest 3 supersoft source candidates are presented in Figure 8. Detected events have been binned on 1000 sec intervals.

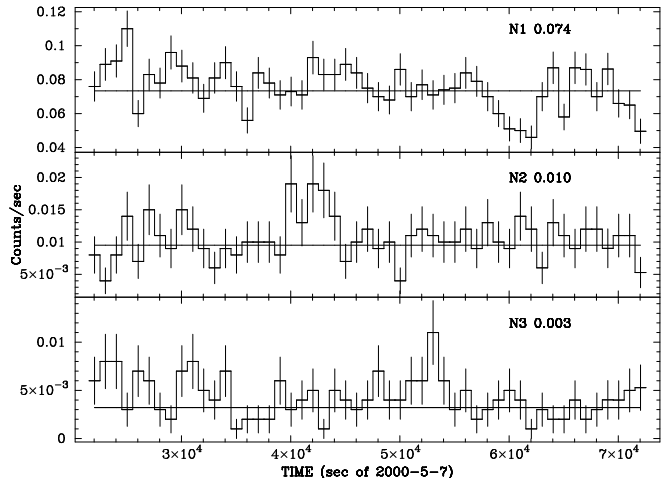


FIG. 8.— *Chandra* light curve of the brightest supersoft source candidates binned on 1000 sec intervals. All standard-grade events in the 0.2–2.0 keV bandpass, within valid good-time intervals, and within the same spatial regions as used for spectral analysis, are included. Error bars represent 1σ statistical uncertainties. Background contributions are negligible: Typical background count rates are 10^{-6} counts s^{-1} pixel $^{-1}$. Labels denote source number and average count rate obtained by fitting a constant to the data (shown as horizontal lines through the data).

The observation was of sufficient duration that the Kolomogorov-Smirnov statistic can be evaluated for the brightest sources to test the hypothesis that the sources are constant. The test shows sources N1 and N2 are variable at high confidence but the remaining sources contain insufficient data to be conclusive. Power spectra were also generated for the brightest sources to search for pulsations or other periodic behavior. Only source N1 had sufficient signal to obtain significant results. No periodicity was detected.

An additional 2.4 ks ACIS-S imaging observation of M81 obtained on 2000 Mar 21, 47 days previous to the 50 ks observation, was acquired through the *Chandra* X-ray Center data archive. Source N1 is the only supersoft source candidate with a sufficient number of counts in this short exposure for analysis. The light curve of source N1 during this observation, binned on 300 sec intervals, is shown in Figure 9. Also shown are the corresponding light curves in the energy bands 0.2–0.5 and 0.5–1.0 keV and the time dependence of the background during the observation. The source brightness declines from a maximum at the beginning of the observation to a statistically insignificant level within ~ 900 s and remains at this low level for the remainder of the observation. No other (bright) source displayed similar changes in X-ray flux during the 2.4 ks observation.

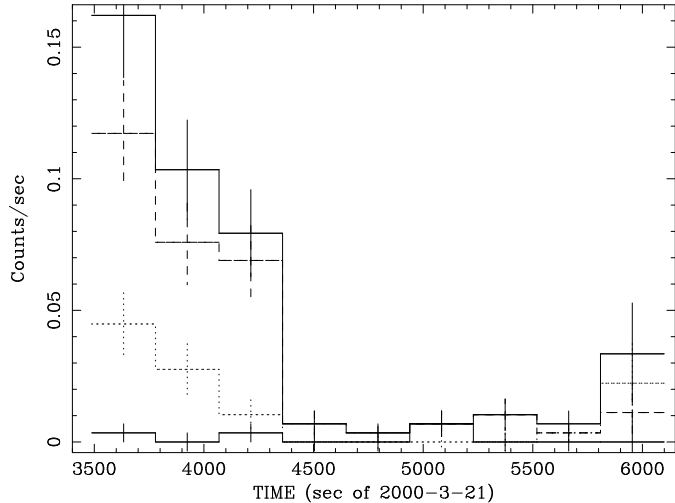


FIG. 9.— *Chandra* 2ks light curve of source N1 binned on 300 sec intervals. The uppermost curve includes all standard grade events in the 0.2–2.0 keV band, the next lower curve represents the 0.5–1.0 keV band (*dashed*) followed by the 0.2–0.5 keV band (*dotted*). The lower curve represents the nearby background scaled by the ratio of the source to the background area. Error bars represent 1σ statistical uncertainties.

The dramatic drop in flux suggests an eclipse event. The observation interval is too short to establish a brightening of the source signifying the end of the eclipse (the observation ended 100 sec into the last interval and this interval contains 4 counts, one of which is probably a background photon based on its PI value). No similar feature is detected in the longer *Chandra* observation and no similar feature can be seen in the relatively poor signal-to-noise *ROSAT* data discussed below.

Assuming the drop in flux signals the onset of an eclipse of an $\sim 1 M_{\odot}$ compact object, that Roche-lobe overflow from the companion is occurring, that the eclipse duration exceeds 1600 s, and that no eclipse occurs during the 50 ks exposure, weak constraints on the orbital elements of any binary system can be derived. These constraints are easily met by massive companions ($\gtrsim 3 M_{\odot}$) that have evolved off the main sequence. Systems in this mass range have periods greater than ~ 1.6 days and eclipse fractions of order 15%. Missing an eclipse is then quite likely though witnessing the onset of an eclipse in a short exposure would be fortuitous. Furthermore, such companion stars should be visible in the *Hubble* images (§2.2). A more likely scenario for supersoft sources is a slightly-evolved main sequence donor in the mass range 1.3–2.5 M_{\odot} (van den Heuvel et al. 1992) or a “helium Algol” with a few-solar-mass companion at the onset of He accretion (Iben & Tutukov 1994, Yungelson et al. 1996). Orbital periods range from 10 hr to 30 hr for the main sequence donor scenario and < 20 hr for the He-accreting systems (Yungelson et al. 1996). There is at best a one-in-three chance that no eclipse is observed during a 50 ks (13.9 hr) observation of systems with a 30 hr period and the probability decreases for the shorter-period systems. Thus, though an eclipse cannot be excluded by the X-ray observations it is not very likely.

Assuming the source is exiting an eclipse phase during the last ~ 300 s of the short exposure, then the eclipse lasts only of order 1800 s. The orbital period must then be of

order a few hours only since $\sim 15\%$ of the period is spent in eclipse. A period this short could not be missed in the 50 ks observation.

Alternatively, nuclear burning on the surface of a WD may be occurring through weak shell flashes that either cause expansion which quenches burning or expels material which obscures the underlying atmosphere as it cools with more violent flashes followed by a larger flux decline. This may explain the Figure 9 light curve where the X-ray flux is roughly a factor-of-two brighter during the onset of the observation than the average value observed during the 50 ks observation (Figure 8). Fitting an exponential to the first 1000 s of this light curve gives an e-folding timescale of ~ 350 s. This is comparable to the sound crossing time over the surface of a WD for reasonable estimates of the sound speed in the burning layer. A change in accretion rate may also trigger large excursions in the X-ray brightness. Southwell et al. (1996) have suggested this mechanism may explain the factor of ~ 20 rise in X-ray flux observed (Schaeidt, Hasinger, & Trümper 1993) in the supersoft source RXJ 0513.9-6951. However, the timescale for contraction of the photosphere leading to the required change in T_{eff} is of order days (Livio 1992). RXJ 0513.9-6951 is probably a low-mass WD system with a correspondingly low X-ray luminosity (Greiner 2000b) far below that observed for source N1.

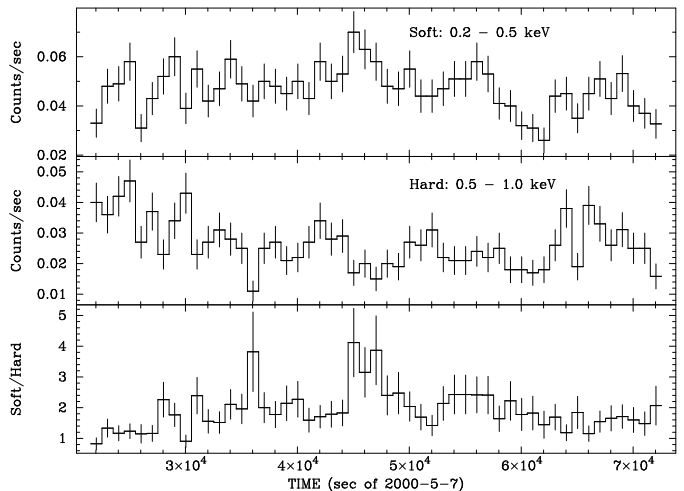


FIG. 10.— *Chandra* 50 ks light curve of source N1 in the 0.2–0.5 keV (*top*) and the 0.5–1.0 keV (*middle*) energy bands binned on 1000 sec intervals. The bottom panel displays the ratio of the two energy bands. Error bars represent 1σ statistical uncertainties.

Interestingly, the spectrum is substantially harder and the brightness is higher during the bright portion of the 2.4 ks observation compared to the 50 ks observation. There is even some flux above 1.0 keV in the 2.4 ks data. The mean photon energy during this bright phase is ~ 730 eV while during the 50 ks observation the mean is ~ 475 eV (Figure 5). Part of the spectral hardening, including most of the flux above ~ 1.1 keV, is caused by pileup in the high rate data. Nevertheless, the spectrum is definitely harder (or, hotter in the context of blackbody spectral models) during this bright phase. There is no clear signature of increasing absorption as the source enters the low rate region of the 2.4 ks light curve as would be

expected in the onset of an eclipse. No other source shows a similar harder spectrum during the 2.4 ks observation.

The other alternative discussed previously in the context of spectral models for source N1 is X-ray emission from an accretion disk around a mid-mass black hole. Variability on many timescales is observed in both massive black holes (AGNs) and in stellar-mass black holes (X-ray transients). Variability is generally caused by instabilities in the disk structure and changes in the accretion flow and is usually accompanied by spectral evolution among high soft states and low hard states. The 50 ks light curve of source N1 in each of two energy bands is shown in Figure 10 along with the ratio of the soft band to the hard band. This shows that source N1 varies differently in different energy bands but it does not help distinguish between standard supersoft source and mid-mass black hole scenarios.

4.2. Long-Term Variability

The fluxes observed by *Chandra* suggest the brightest 4 or 5 supersoft source candidates may be detectable in archival *ROSAT* observations of the field. M81 was observed 9 times by *ROSAT*/PSPC over the interval 1991 March through 1994 April and 11 times by *ROSAT*/HRI from 1992 Oct through 1998 April. Source N1 is present in *ROSAT*/HRI images but is too near the bright nucleus of M81 to be resolved in *ROSAT*/PSPC data. Source N2 is clearly present and isolated from other X-ray sources in both PSPC and HRI observations. Source N3 is confused with a bright nearby object in both *ROSAT* instruments. Source N4 is likewise too near the nucleus for positive detection. Source N5 is marginally detected at the 2.8σ level in the longest of the HRI exposures. This corresponds to a *Chandra* luminosity of $\sim 2 \times 10^{37}$ erg s $^{-1}$, consistent with a constant source luminosity between the two observations. The remaining sources are too weak to be detected at a reasonable confidence level. The entire *ROSAT* dataset has been independently analyzed by Immler & Wang (2001). *Chandra* source N1 is within $3.''2$ of HRI source H25 of Immler & Wang (2001) and is listed as a variable source with no other comment. Source N2 is within $3.''3$ of HRI source H36 which is coincident with PSPC source P44. Source P44 is a soft source based on its PSPC hardness ratios (Immler & Wang 2001). No other *Chandra*-detected supersoft source candidate is among the *ROSAT* sources identified by Immler & Wang (2001).

The combined *ROSAT*/HRI, PSPC, and *Chandra* light curves of sources N1 and N2 are displayed in Figure 11. Here, the average count rate of each individual observation is shown combined to form each data point. The *Chandra* and *ROSAT*/PSPC observed count rates have been scaled to *ROSAT*/HRI observed count rates using the PIMMS tool (Mukai 1993) and assuming spectral properties for the two sources as derived in section 3. This scaling can account for some of the disparity seen, for example, in the lower panel of Figure 11 (source N2) where the PSPC data and the two *Chandra* points are lower than the intervening *ROSAT*/HRI fluxes. Nevertheless, both sources are clearly present in the data spanning >7.5 yr. As discussed in the next section, this fact limits the possibility that these sources could be classical novae.

⁶The bulge is defined here as the region interior to the inner Lindblad resonance at radius 4 ± 0.2 kpc (Kaufman et al. 1989 and references therein). This is larger than the bulge radius (2.55 kpc) adopted by Tennant et al. (2001) resulting in 13 more X-ray sources within the bulge.

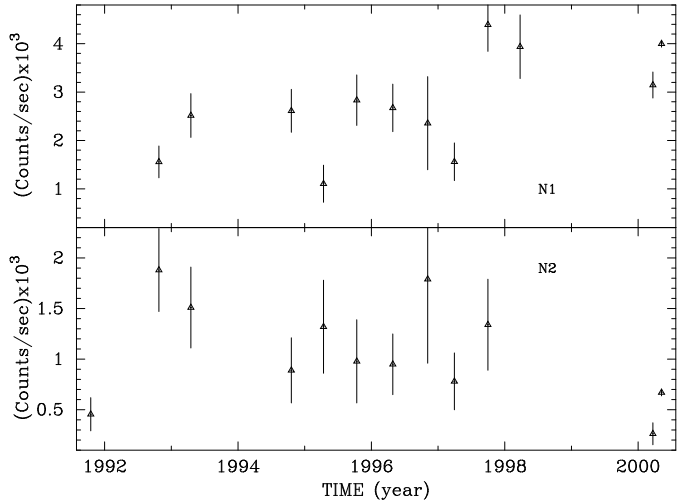


FIG. 11.— Combined *ROSAT* and *Chandra* light curves for Source N1 (upper panel) and N2 (lower panel). Count rates have been scaled to *ROSAT*/HRI count rates assuming the spectral parameters derived in §3 from the 50 ks *Chandra* data. *ROSAT*/HRI data are marked by squares, *ROSAT*/PSPC data with triangles, and *Chandra* data with circles. Errors denote 1σ statistical uncertainties. Labels denote average observed count rates.

5. DISCUSSION

Supersoft sources are a well-established class of X-ray emitting objects. Of the 19 well-studied systems (e.g., Greiner 2000a), all within the Galaxy or the Magellanic Clouds, nine are accreting WDs in close binaries (CBSS) that are nuclear burning accreting material in a steady state, four are classical or recurrent novae, three are symbiotic systems, and one is a planetary nebula nucleus. The common source of X-ray emission among these sources is nuclear burning either of accreting material (in a steady state or in a nova flash) or of residual fuel (following, e.g., the formation of a planetary nebula).

The assumption that all supersoft sources result from nuclear burning on WD stars is adopted here for purposes of discussion. Two questions to be addressed are: (1) Is the observed population and its distribution within M81 consistent with this theory and (2) Are the observed X-ray properties of the individual sources consistent with previously-observed members of this rather heterogeneous class (and, if so, which ones)?

5.1. The M81 Population of Supersoft Sources

Nine supersoft source candidates have been identified in M81 based on broad-band X-ray colors. All are located on the S3 device. Four of these are located in the bulge of M81 and the remainder are aligned with the spiral arms with the exception of one object in the inter-arm disk region. The bulge comprises 30% of the area of the S3 device⁶ thus 2.7 of the 9 supersoft sources should occur in the bulge if the spatial distribution were uniform on S3. However, 54 of the 97 X-ray sources of all types on S3 are located in the bulge (Tennant et al. 2001) and therefore 5 supersoft sources would be expected there if the supersoft sources follow the general distribution of X-ray sources. Twenty-one of the 43 disk X-ray sources are aligned with the spiral arms while 4 of the 5 supersoft disk sources are on the arms.

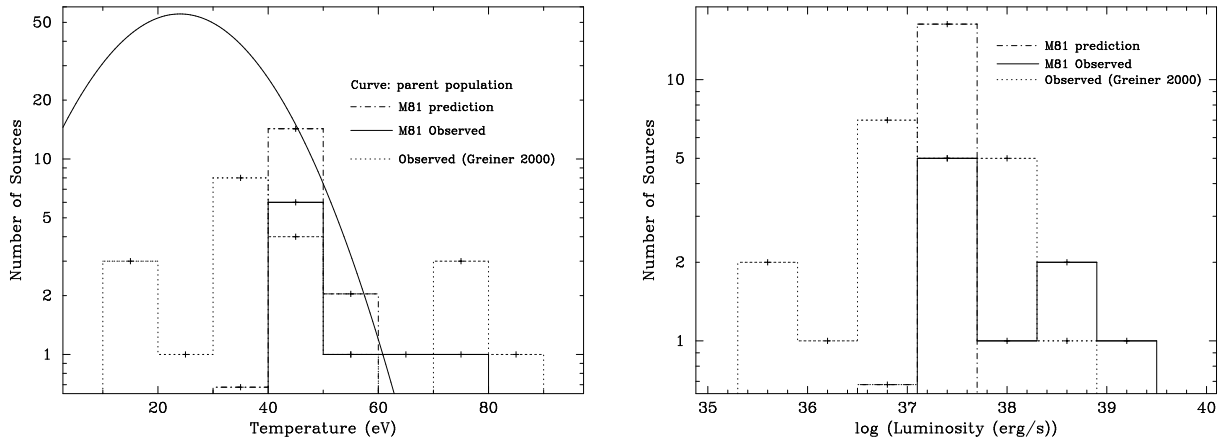


FIG. 12.— Distribution of supersoft source systems over effective temperature (*left*) and bolometric luminosity (*right*). Shown are the predicted and observed distributions for the galaxy M81 (see text) and the distribution of known sources in the Galaxy and Magellanic Clouds as catalogued by Greiner (2000a). The M81 predicted distributions assume the sources are distributed normally over both temperature and luminosity. This normal distribution is the curve in the left panel. For clarity, the corresponding distribution is omitted from the right panel as it appears as a narrow asymmetric curve centered on 3×10^{37} erg s $^{-1}$ in the logarithmic scaling used here.

The observed properties of the supersoft sources in M81 favor high mass WD systems ($M_{WD} \sim 1.0 M_{\odot}$) and hence a younger population of progenitor stars (zero-age main sequence mass $\sim 7 M_{\odot}$). This favors locations near star forming regions such as spiral arms. Conversely, the interstellar absorption is relatively higher in the spiral arms than in the disk or bulge which would tend to obscure the lowest-temperature supersoft sources. Indeed, the two supersoft sources located on the spiral arms with sufficient counts for spectral fitting (N2 and N3) have relatively high X-ray absorbing columns and temperatures of 50–60 eV.

Objects in the bulge are expected to be an older population (>9 Gyr, e.g., Kong et al. 2000) except in the central $\sim 50''$ where an enhancement in recent star formation activity is suggested by UV (Hill et al. 1992, Reichen et al. 1994) and H α (Devereux, Jacoby & Ciardullo 1995) imaging and consistent with the concept of gas-fall toward the center of M81. This may have begun as recently as ~ 400 Myr ago as a result of an encounter with NGC 3077 (Thomasson & Donner 1993) or M82 (de Grijs, O’Connell, Gallagher 2001). All the bulge supersoft source candidates lie outside this central region and appear to have relatively low absorbing columns consistent with the lack of gas and dust. The standard supersoft source model (van den Heuvel et al. 1992) requires companion stars in the mass range 1.3–2.5 M_{\odot} to maintain steady nuclear burning of accreting H on the surface of the WD. Stars of this mass range evolve from the main sequence on timescales of order several 10^8 to greater than 10^9 years and so the required accretion could be occurring in the current epoch in the bulge if the donor stars were formed in an encounter.

How many supersoft sources are expected in the 50-ks *Chandra* observation? Di Stefano & Rappaport (1994) estimated the number of supersoft sources in external galaxies observable by *ROSAT* by carefully accounting for the effects of interstellar absorption on an assumed parent population taken from the work of Rappaport, Di Stefano, & Smith (1994). The parent population was that of systems

whose luminosities and temperatures matched the steady-burning regime computed by Iben (1982). This omits several classes of supersoft source including wind-driven symbiotic systems, novae, and recurrent novae. Nevertheless, it is possible to apply the basic approach of Di Stefano & Rappaport (1994) to the *Chandra* observation of M81. Scaling from their estimate of the total population of supersoft sources in M31 by the ratio of blue luminosities [*i.e.*, assuming supersoft sources contain massive WDs and hence evolved from a young stellar population (Motch, Hasinger, & Pietsch 1994, Di Stefano & Rappaport 1994)], a total of 1700 supersoft sources are expected in M81.

To estimate the fraction detectable by *Chandra*, the population distributions in temperature and bolometric luminosity as derived by Rappaport, Di Stefano, & Smith (1994) can be roughly approximated by normal distributions with means $T = 24$ eV and $L = 3 \times 10^{37}$ erg s $^{-1}$ and standard deviations of 13 eV and 8.5×10^{36} erg s $^{-1}$, respectively (see also Fig. 3 of Di Stefano & Rappaport 1994). By randomly sampling values of T and L from these two independent distributions, assuming a blackbody spectrum and a modest column of $N_H = 8 \times 10^{20}$ cm $^{-2}$ (twice the Galactic value), and using the PIMMS software tool (Mukai 1993), the predicted *Chandra* observed count rate distribution can be accumulated. Assuming 20 counts in a 50-ks observation as a detection threshold, only 1% of the supersoft sources in M81 should be detectable with the BI device S3.

As the viewing field of S3 encompasses 23% of the D_{25} area of M81, ~ 4 of the 1700 supersoft sources in the parent population should be detected in the 50-ks observation on S3. This is consistent with the observed population of 9 sources in light of the large uncertainties involved including a factor-of-two uncertainty in the normalization of the parent population (Di Stefano & Rappaport 1994) and the neglect of other classes of supersoft source systems by these authors (Yungleson et al. 1996).

The simulation also shows that only systems with temperatures $T \gtrsim 40$ eV and bolometric luminosities $\sim 2 \times$

10^{37} erg s $^{-1}$ are likely to be detected by *Chandra*. This result can be compared to the distribution of temperatures and luminosities reported in Greiner (2000a) for 21 supersoft sources (two of which have not been optically classified) and to the 9 supersoft sources discovered in M81. Figure 11 shows this comparison. (For brevity, it has been assumed here that the 6 weakest supersoft sources in M81 all have temperatures of 45 eV, see §3.4.) The distributions of the Greiner (2000a) sample are clearly broader than predicted or observed for M81. This is a consequence of the greater diversity of local environments in which these sources are found and the dissimilar instruments used to investigate them. The peak of the observed M81 distributions in temperature and luminosity coincide with the predicted distribution but these peaks are dominated by the weak sources and are, therefore, highly uncertain. The bright observed sources are, however, located at higher temperatures and luminosities than expected.

5.2. The Nature of Individual M81 Supersoft Sources

5.2.1. Source N1

By far the brightest supersoft source candidate in the sample lies within the bulge of M81 approximately $52''$ from the nucleus. Its spectrum is well-fit with a simple blackbody model of 78 – 86 eV ($T \sim 9 \times 10^5$ K) with a modest absorption ($N_H \sim 6 \times 10^{20}$ cm $^{-2}$) resulting in an implied bolometric luminosity exceeding 10^{39} erg s $^{-1}$. Although the bolometric luminosity is highly uncertain, even the observed luminosity exceeds the Eddington limit for a Chandrasekar-mass WD.

The brightest well-studied supersoft sources are typically novae or recurrent novae with peak bolometric luminosities often exceeding 10^{38} erg s $^{-1}$. One of the best examples is U Sco. Kahabka et al. (1999) investigated BeppoSAX observations of this recurrent nova taken ~ 20 days after the peak of the most recent optical outburst. They find a temperature of $\sim 9 \times 10^5$ K and a bolometric luminosity of up to 2×10^{38} erg s $^{-1}$ from a combination of non-LTE atmosphere models and an optically-thin thermal emission component, assumed to arise from a wind, added to fit the ~ 1 – 2 keV portion of the observed spectrum.

Although source N1 has X-ray properties similar to those of U Sco, it is unlikely that source N1 is a nova. Novae occur in systems with relatively low mass transfer rates where a layer of fuel is accumulated for a period of time before compressional heating causes ignition. The mass of the accumulated layer increases with decreasing WD mass. Consequently, the X-ray light curves evolve slowly, lasting up to 10 years or so, in systems with low-mass WDs. The luminosity is proportional to the WD mass M_{WD} , $L_{bol} \sim 1.8 \times 10^{38} (M_{WD} - 0.26)$ erg s $^{-1}$ assuming H accretion, where M_{WD} is measured in solar units (Iben & Tutukov 1989). Thus the luminosity is low for these long-lived low M_{WD} novae and the recurrence time between events is very long. Conversely, systems containing high mass WDs, such as inferred for U Sco, have a higher peak luminosity but are short-lived X-ray sources (~ 0.1 yr, *e.g.*, Kato 1997). The recurrence times are also shorter but are still of order years and therefore inconsistent with the observed light curve of source N1. (Note the short- and long-term variations observed in the X-ray

light curve of source N1 are better described as transience or variability in contrast to recurrence as applied to novae.)

At higher accretion rates is a regime of steady-state burning of accreting material. The maximum luminosity in the steady-burning regime is $L_{bol} = 2.3 \times 10^{38} (M_{WD} - 0.5)$ erg s $^{-1}$ and occurs at the maximum accretion rate $\dot{M} = 7.8 \times 10^{-7} (M_{WD} - 0.5) M_{\odot}$ -yr $^{-1}$ (Iben 1982, again assuming H-rich accretion). The highest temperatures, up to ~ 85 eV, are obtained by the highest mass WDs as are the highest luminosities. However, an accretion rate of $\sim 5 \times 10^{-6} M_{\odot}$ -yr $^{-1}$ is needed to obtain the bolometric luminosity inferred for source N1 assuming steady burning. At such high accretion rates, however, the photospheric radius expands to red giant dimensions; only a fraction of the fuel is consumed; and the X-ray emission, formed in a thin layer at the base of the envelope, is hidden by the overlying material. The burning may instead drive a strong, opaque wind (Hachisu, Kato & Nomoto 1996). If the outcome of a high mass transfer rate is formation of an envelope then this system should be observable optically as a hot giant or red giant star, contrary to the *Hubble* observations (§2.2) and not as a strong X-ray source. If the accretion drives a wind, then the photospheric temperature is only $T \sim 10^5$ K. However, if the accretion rate *decreases* the wind mass-loss rate will decrease as will the effective photospheric radius. Regions closer to the burning layer will become exposed and the X-ray temperature and X-ray luminosity will increase dramatically (Hachisu, Kato, & Nomoto 1996). The subsequent evolution of systems of this type were not followed by Hachisu, Kato, & Nomoto (1996).

If the accreting material is He-rich, then the system can sustain a higher mass transfer rate while remaining in the steady nuclear-burning regime (Iben & Tutukov 1989). The increase in mass transfer rate by roughly an order of magnitude translates into only a factor of 2 or so higher luminosity because of the lower specific energy generation rate of He relative to H so that the maximum luminosity is $L_{bol} \sim 4.6 \times 10^{38} (M_{WD} - 0.58)$ erg s $^{-1}$ (Iben & Tutukov 1989). Although He-rich LTE white dwarf atmosphere models failed to provide a satisfactory fit to the observed spectrum, He-rich accretion remains an attractive scenario for source N1 because the Eddington limit luminosity for He accretion is twice that for H. Helium accretion can occur during a second phase of mass transfer to the compact star when the companion has exhausted He in its core (Iben & Tutukov 1994). The donor star in this scenario is either the nucleus of an early asymptotic giant branch or an evolved He-star remnant with a CO core. Under appropriate conditions, this mass transfer can be conservative (Iben & Livio 1993) instead of lost in a common-envelope process (Iben & Tutukov 1985). The initial mass of the donor star tends to be rather large in this scenario, ~ 6.5 – $9.5 M_{\odot}$ for steady burning, so that such systems should be rather rare in the old population of bulge stars in M81. Helium tends to burn explosively (Sion & Starfield 1993) unless the helium layer can be maintained at a high temperature (Josè et al. 1993). A series of weak He shell flashes may occur for systems near the stability limit producing luminosities of order $\sim 4 \times 10^{38}$ erg s $^{-1}$, and temperatures ~ 70 eV (Iben & Tutukov 1994). These systems

tend to have less than ~ 20 hr orbital periods (Yungelson et al. 1996), comparable to or less than those of subgiant donors in H-accreting systems and of main sequence stars losing mass on a thermal timescale (~ 1 day orbital periods, van den Heuvel et al. 1992). Another channel for He accretion is a semidetached double degenerate system in which the secondary is a helium WD (Iben & Tutukov 1989). Such a system must have an orbital period of order minutes (Verbunt & van den Heuvel 1995).

In short, none of the standard nuclear-burning WD scenarios predict luminosities as high as that inferred for source N1. However, theoretical treatments have not rigorously explored the behavior of these systems in regimes beyond the stability limit. Other alternatives exist. Neutron star binaries often exhibit a luminous thermal component though rarely as soft as observed here (and hence one of the original motivations for the nuclear-burning WD scenario for supersoft sources, van den Heuvel et al. 1992). One exception is the Be/X-ray binary RX J0059.2-7138 with $T_{eff} \sim 36$ eV (Hughes 1994) though this source is accompanied by a strong power law component extending the spectrum beyond the *ROSAT* band. Weakly magnetized neutron stars such as the X-ray burst sources, tend to have correspondingly weak power law spectral components but also have high characteristic temperatures during the burst phase (e.g., Lewin, van Paradijs, & Taam 1995). Similarly, typical black hole binaries display a “soft” component with characteristic temperature > 1 keV and a hard power law component.

A completely different scenario that may explain the observed X-ray properties of source N1 is X-ray emission from an optically-thick accretion disk surrounding a mid-mass black hole. The most attractive feature of this model is that the implied bolometric luminosities derived here are a small fraction of the Eddington limit. The observed X-ray spectrum is consistent with that from the innermost disk radius assuming the central object has a mass $M_{BH} \sim 1200 / (\cos i)^{1/2}$. While no objects in this mass range have been confirmed, invoking the Eddington limit to X-ray-bright sources has led to suggestions of masses in excess of 10-100 M_{\odot} , in many instances (e.g., Makishima et al. 2000) and as high as $\sim 700 M_{\odot}$ in the case of a luminous source in M82 (Kaaret et al. 2001, Matsumoto et al. 2001).

5.2.2. Source N2

Source N2 has a distinct edge at ~ 870 eV well fit by O VIII absorption in the LTE atmosphere model. This feature is commonly found in the hotter supersoft sources such as the LMC source CAL 87. Ebisawa et al. (2001) find a temperature of 75 eV for CAL87 from *ASCA* observations with an absorbing column comparable to that obtained here for source N2 ($N_H \sim 2 \times 10^{21} \text{ cm}^{-2}$).

Parmer et al. (1997) report BeppoSAX observations of CAL 87 are equally well-fit with either blackbody, LTE, or NLTE atmosphere models with temperatures ranging from 42 eV for the blackbody fits to 57 and 75 eV for their LTE and NLTE models. The blackbody model implies $L_{bol} \sim 4 \times 10^{38} \text{ erg s}^{-1}$ but the LTE and NLTE fits are consistent with more modest luminosities, $\sim 3\text{--}5 \times 10^{36} \text{ erg s}^{-1}$. Including the O VIII absorption edge increases the blackbody temperature and decreases the bolometric luminosity to values similar to their NLTE models.

This trend is opposite to the results reported here for source N2: blackbody models predict higher temperatures than the LTE models and bolometric luminosities comparable to or lower than the LTE models. The best-fit model, LTE with 1% of solar metal abundance, has a temperature of 67 eV and a hydrogen column density of $1.6 \times 10^{21} \text{ cm}^{-2}$ very similar to CAL 87. The observed luminosity is $3.9 \times 10^{37} \text{ erg s}^{-1}$ and $L_{bol} \sim 5.3_{-2.1}^{+4.8} \times 10^{38} \text{ erg s}^{-1}$, much higher than the models of Parmer et al. (1997) predict but consistent (within the large uncertainties) with the highest luminosity reported by Ebisawa et al. (2001) for CAL 87.

CAL 87 is a close binary system that exhibits eclipses with a period of 10.6 hours. The eclipses are visible as shallow dips in the X-ray light curve. Small-amplitude variability of this kind cannot be distinguished in the relatively low-quality light curve of source N2.

5.2.3. Source N3

This source is also relatively highly absorbed but considerably cooler than the two brightest sources with $T_{eff} \sim 50$ eV. This value is more typical of many of the well-studied supersoft sources (Figure 5.1, Greiner 1996, 2000a), such as the CBSS sources CAL 83 and 1E 0035.4-7230. Parmer et al. (1998) report acceptable fits can be achieved with blackbody, LTE, or NLTE atmosphere models applied to BeppoSAX observations of CAL 83. Their resulting temperatures are ~ 45 eV for the blackbody and LTE models and ~ 33 eV for their NLTE fits. As with source N3 (§3.3), Parmer et al. (1998) report the low temperature and consequent lack of strong absorption edges does not allow a distinction to be made among the models (see also Figure 4). BeppoSAX and *ROSAT* observations of 1E 0035.4-7230 (Kahabka, Parmer, & Hartmann 1999) again do not allow either blackbody, LTE, or NLTE models to be discounted though in this case a feature ascribed to C V and C VI absorption is evident. Temperatures derived by Kahabka, Parmer, & Hartmann (1999) range from $\sim 40 \pm 13$ eV from their blackbody fits to $\sim 28 \pm 4$ eV from their NLTE model fits to 1E 0035.4-7230. Both CAL 83 and 1E 0035.4-7230 derived bolometric luminosities are of order a few times 10^{37} , roughly an order of magnitude lower than the best-fit values derived here for source N3 though within the large uncertainties in the latter.

5.2.4. Source N4 and N5

Though little can be said about the X-ray properties of these two sources beyond their broad-band classification as supersoft source candidates, these objects may be similar to the LMC source CAL 83.

Source N4 and N5 are spatially coincident with objects ID 68 and 116, respectively, in the list of [OIII] $\lambda 5007$ Å sources observed by Jacoby et al. (1989). This emission line is also prominent in the optical images of CAL 83 (Remillard et al. 1995) and is attributed there to ionization in the interstellar medium by a large UV and soft X-ray photon flux from the central source. Rappaport et al. (1994) modeled the ionized regions surrounding supersoft sources and calculated resulting optical line intensities. The strongest predicted lines are the [OIII] $\lambda 5007$ Å and HeII $\lambda 4686$ Å lines. Adopting the foreground extinction to M81 from Jacoby et al. (1989), their observed [OIII] $\lambda 5007$ Å fluxes are consistent with those expected from the

supersoft source models. For example, the $\lambda 5007 \text{ \AA}$ flux from object ID 116 is $\sim 4 \times 10^{-16} \text{ erg cm}^{-2} \text{ s}^{-1}$ while Rappaport et al. (1994) predict $1.6 \times 10^{-16} \text{ erg cm}^{-2} \text{ s}^{-1}$ and $2.3 \times 10^{-15} \text{ erg cm}^{-2} \text{ s}^{-1}$ from models with intrinsic luminosities of 10^{37} and $10^{38} \text{ erg s}^{-1}$, respectively, and source temperatures of $4 \times 10^5 \text{ K}$.

Parmar et al. (1998) find a temperature $T_{eff} \sim 30\text{--}50 \text{ eV}$ for CAL 83 and $L_{bol} \sim 4 \times 10^{37} \text{ erg s}^{-1}$. These values are within the estimated values for sources N4 and N5.

A PNe cannot be excluded based on the X-ray and [OIII] fluxes of sources N4 and N5. The central stars of PNe can have luminosities as high as that inferred for sources N4 and N5 but only the most massive central stars are hot enough to be detected in soft X-rays (e.g., Paczynski 1971). This is the case for the SMC supersoft source 1E00056.8-7154. This source is coincident with PNe N67 (Wang 1991) but is anomalously X-ray bright for a PNe [$T_{eff} \sim 38 \text{ eV}$, $L_{bol} \sim 2 \times 10^{37} \text{ erg s}^{-1}$ (Brown et al. 1994, Heise et al. 1994)]. Unfortunately, no obvious spectroscopic distinction between PNe and supersoft sources has been identified (Di Stefano, Paerels, & Rappaport 1995).

5.2.5. Other Sources

The X-ray evidence in support of a supersoft source nature of the remaining candidates is based entirely on their X-ray colors. Their spectra and light curves are of insufficient quality for detailed analysis.

As there is no long-term X-ray light curve for these sources, their identification as novae cannot be ruled out. The rate of nova occurrence in M81 is roughly 20 yr^{-1} (Della Valle & Livio 1994) and, as discussed above, X-ray lifetimes range from months for the brightest sources up to ~ 10 years. For the values of L_{bol} estimated in §3, 10^{37} to $4 \times 10^{37} \text{ erg s}^{-1}$, the corresponding WD masses are low, $M_{WD} \sim 0.3$ to $0.5 M_{\odot}$. These masses correspond to long-lived novae, typically radiating as a (very soft) X-ray source for $\sim 7 \text{ yr}$ for $M_{WD} = 0.6 M_{\odot}$ (Kato 1997). Visual magnitudes of novae can be as high as $m_V \sim 22$ to 23 at the distance of M81 but the visible light rapidly declines after maximum light as the spectrum hardens and the X-ray flux rises. A $0.6 M_{\odot}$ WD nova, for instance, only becomes X-ray visible $\sim 4 \text{ yr}$ after optical outburst.

The weak supersoft source candidates could also be steady-burning CBSS systems. The estimated L_{bol} corresponds to a range of WD masses $M_{WD} \sim 0.7$ to $\lesssim 1.0$. However, WDs in this mass range should be considerably cooler ($T_{eff} \lesssim 40 \text{ eV}$) than the $40\text{--}50 \text{ eV}$ temperatures suggested by the instrumental selection effect. Below $M_{WD} \sim 0.65 M_{\odot}$, the photospheric radius expands in the steady nuclear burning case and T_{eff} plummets (Iben 1982). Thus only a narrow range of masses are possible for the weak supersoft sources if they are steadily burning their accreted hydrogen.

Another evolutionary channel leading to the formation of a supersoft source is wind-driven accretion in symbiotic systems (Sion & Starrfield 1994). These systems can undergo H shell flashes, reach luminosities of order $\sim 10^{37} \text{ erg s}^{-1}$, and remain at this plateau for $\sim 250 \text{ yr}$ in some circumstances. For many of the low-mass WDs modeled by Sion & Starrfield (1994), the flashes are weak, the envelope radius remains compact, and the resulting photospheric temperature is relatively high. However, the maximum temperatures achieved were $T_{eff} \sim 20 \text{ eV}$. The

supersoft source SMC 3 (RX J0048.4-7332) is a symbiotic nova of this type. Jordan, et al. (1996) derive a luminosity $L_{bol} \sim 4 \times 10^{37} \text{ erg s}^{-1}$, a temperature of 22 eV , and a mass of $\sim 0.8 M_{\odot}$ for this object. The weak supersoft source candidates are unlikely to be symbiotic systems because of the difficulty detecting objects of such low temperatures in M81 with *Chandra*. An archival *Chandra* observation of AG Dra, for instance, detects very little flux above $\sim 0.3 \text{ keV}$.

6. SUMMARY & PROSPECTS

6.1. *Chandra* Observations of M81

An important part of the *ROSAT* legacy has been the identification of supersoft sources as a phenomenologically distinct class of X-ray emitting object. The *Chandra* X-ray Observatory affords an excellent opportunity to extend the study of supersoft sources to other nearby galaxies.

As a first step, the population of supersoft source candidates discovered in M81 has been investigated. The number of supersoft sources detected and their spatial distribution are consistent with population synthesis estimates. X-ray spectral analysis shows the M81 sources are qualitatively similar to previously-studied supersoft sources though the brightest M81 sources tend to be hotter and more luminous than is typical of the class. This was shown to be, in part, a natural consequence of the higher sensitivity of *Chandra* to the high-temperature region of the supersoft source distribution.

Bolometric luminosities deduced here from the spectral fits often exceed the Eddington limit for spherical accretion onto a $1.4 M_{\odot}$ star. Such extreme luminosities lie beyond the previously-observed distribution of supersoft sources and, more importantly, cannot be reconciled with prevailing theories for supersoft sources as WDs powered by stable, steady-state, surface nuclear burning. But, the study of supersoft sources with the *Chandra* Observatory is still in its infancy. Important uncertainties remain. As in the *ROSAT* era, spectral modeling remains problematic. Simple blackbody models, like those used in this work, are known to greatly overestimate bolometric luminosities in some cases. LTE model atmospheres, also applied here, are appropriate when a well-defined photosphere is present such as in the high density gradient at the surface of a WD. Even this model fails when the nuclear burning is near the stability limit, the atmosphere becomes extended, and a wind drives mass loss as may be the case in the brightest supersoft source candidate in M81. In addition, the energy calibration of the BI devices at low photon energies is uncertain and could also have a significant effect on the results reported here.

Many of these uncertainties may be resolved or at least mitigated as pending *Chandra* observations of well-studied supersoft sources are analyzed and compared to previous observations and to specific theoretical expectations. High-resolution grating spectroscopy will be indispensable in this regard as many of the calibration uncertainties can be circumvented while, at the same time, models for the X-ray spectra can be more tightly constrained. An example of the richness of such a spectrum is that of CAL 83 obtained by XMM-Newton/RGS (Paerels, et al. 2001). The population of supersoft source candidates discovered in M81 also reveals the value of isolating sources to inves-

tigate their local environments and of obtaining precise locations for future observations at X-ray and other wavelengths.

In spite of the current uncertainties, the remarkable properties deduced for the brightest supersoft source candidate in M81 should not be overlooked. This source exhibits large variations in X-ray brightness on timescales of order hours yet maintains a high average X-ray brightness throughout the roughly 8 year span of combined *ROSAT* and *Chandra* observations of the region. In the context of the nuclear burning WD scenario, its high temperature and luminosity imply a high mass, near the Chandrasekhar limit for WDs, and a high accretion rate, above that for steady-state nuclear burning. While optical monitoring would be difficult, at best, future observations are strongly encouraged to more fully understand this source. The accurate location provided in Table 1 should aid substantially in this regard.

6.2. Observations of Other Galaxies

The most extensive study of supersoft sources in an external spiral galaxy similar to our own and M81 is the *ROSAT* survey of M31 (Supper et al. 1997, Kahabka 1999). Based on hardness ratios, Supper et al. (1997) identified 15 supersoft source candidates not associated with SNRs or foreground objects in a 6.3 square degree M31 field. Kahabka (1999), using a slightly modified selection criteria, identified an additional 26 candidates in the field. Kahabka (1999) found a total of 7 of the combined 41 supersoft sources are within the ~ 6 kpc bulge of M31 with the remainder evenly distributed over ~ 12 to 25 kpc radii. The lack of detected sources in the region ~ 6 to 12 kpc was explained as a consequence of a higher H column within this annulus. Kahabka (1999) suggests that the spatial distribution favors a disk population of younger stars by comparing to the populations of Cepheids and (older) blue stars. The supersoft source distribution does not follow that of novae which are bulge-dominated and follow the old stellar population found in the bulge. After accounting for possible foreground objects and SNRs, Kahabka (1999) finds 1 bulge source for every 4–7 disk sources. This is marginally less than reported here for M81 where 4 bulge sources were found for an extrapolated total population of $9/0.57 \sim 16$ supersoft sources within the D_{25} area of M81. Kahabka (1999) also estimates the temperatures for all the sources and finds they range from ~ 30 –60 eV, typically, up to ~ 73 eV for the recurrent transient RX J0045.4+4154. This latter source is also one of the brightest with an inferred $L_{bol} \sim 10^{38}$ erg s $^{-1}$ (White et al. 1995).

A more detailed comparison between the supersoft source populations of M31 and M81 must await further analysis of the extensive *Chandra* M31 dataset. Only then can many of the instrumental selection effects be eliminated. In the interim, comparison to other *Chandra*-observed galaxies must suffice.

Numerous deep observations of nearby galaxies have been performed by *Chandra* in the ~ 2 years since its launch. Discovery (or lack thereof) of supersoft source candidates have been reported in the literature for only a few galaxies. Sarazin, Irwin, & Bregman (2000,2001) report 3 supersoft sources in a sample of 90 point sources in the elliptical galaxy NGC 4697 to a limiting luminosity of

$\sim 5 \times 10^{37}$ erg s $^{-1}$ based on hardness ratios. No supersoft sources were discovered in M84, an elliptical galaxy in the core of the Virgo cluster, based on the hardness ratio criteria (Finoguenov, Jones, & Kudritzki 2001). Pence et al. (2001) report the discovery of ten supersoft sources among 110 objects in M101 using color definitions different than those defined here. Pence et al. (2001) combined the spectra of the three most luminous supersoft sources, reportedly having similar spectral shapes, and find a best fit blackbody temperature of 72 ± 2 eV and a mean (unabsorbed) luminosity of 1.4×10^{38} erg s $^{-1}$. These values are similar to the brightest supersoft sources in M81 with the exception of source N1 which has an unabsorbed flux 5–8 times higher. The remaining 7 supersoft sources in M101 have a distinctly softer spectrum. When combined, the best fit blackbody temperature is 47 ± 2 eV and unabsorbed luminosity is $L_X = 1.1 \times 10^{37}$ erg s $^{-1}$ for a column fixed to the Galactic value ($N_H = 1.2 \times 10^{20}$ cm $^{-2}$). Again, these values are consistent with those estimated here for the weak sources in M81 although, as shown above, a temperature of order 40–50 eV is expected on the basis of instrumental selection effects and the shape of the parent population estimated from population synthesis models. The position of only one supersoft source candidate lies within the bulge of M101. However, M101 has a later Hubble type, Scd, and hence a smaller bulge than M81 (Sab) extending only to ~ 0.75 , or approximately 3% of the S3 viewing field analyzed by Pence et al. (2001).

These comparisons are intriguing. They suggest that perhaps there is another supersoft source population of anomalously X-ray bright and hot objects in nearby galaxies similar to our own. Care must be exercised, of course, as there are, to date, only a handful of objects with these properties, no corroborating evidence in support of this conjecture from other wavebands, and no satisfactory theory predicting such extreme X-ray behavior. These comparisons also suggest a trend across the Hubble sequence with fewer supersoft sources in early type galaxies compared to late types. The supersoft sources appear to be associated with the younger population of stars found on spiral arms though some are found in the relatively old population of bulge stars. Irregular galaxies would then have a disproportionate number of supersoft sources. Di Stefano & Rappaport (1994) estimate 125 and 25 supersoft sources are active in the LMC and SMC, respectively, based on their blue luminosities relative to M31. Eight supersoft sources have been observed in the LMC and 4 in the SMC. This suggests either the population estimate is low or the observed fraction is high for these two galaxies. Of course, there is a strong selection bias that must be taken into account.

We thank A. Ibragimov for constructing the WD model atmospheres used in this work, A. Shafter for providing an H α image of the field and for information on nova rates, T. Pannuti for radio data analysis, and M. McCollough for analyzing archival *Hubble*/WFPC2 data. K. W. and V. S. thank M. Weisskopf for funding their visits to MSFC. Support for this research was provided in part by NASA/*Chandra* grant GO0-1058X to D. A. S. and by Russian Basic Research Foundation grant 99-02-17488 to V. S.

REFERENCES

- Anders, E., & Grevesse, N. 1989, *Geochim. Cosmochim. Acta*, 53, 197
- Arnaud, K. 1996, in *Astronomical Data Analysis Software and Systems V*, ASP Conference Series 101, ed. G. Jacoby & J. Barnes (San Francisco:ASP) 17
- Brown, T., Cordova, F., Ciardullo, R., Thompson, R., & Bond, H. 1994, *ApJ*, 422, 118
- de Grijs, R., O'Connell, R. W., & Gallagher, J. S. III 2001, *AJ*, 121, 768
- Della Valle, M., & Livio, M. 1994 *A&A* 286, 786
- Dere, K. P., Landi, E., Mason, H. E., Monsignori Fossi, B. C., Young, P. R. 1997, *A&AS*, 125, 149
- de Vaucouleurs G., de Vaucouleurs A., Corwin Jr. H. G., Buta R. J., Paturel G., Fouque P. 1991, *Third Reference Catalogue of Bright Galaxies (RC3)*, (New York:Springer-Verlag)
- Devereux, N. A., Jacoby, G., & Ciardullo, R. 1995 *AJ*, 110, 1115
- Di Stefano, R., Paerels, F. & Rappaport, S. 1995, *ApJ*, 450, 705
- Di Stefano, R., & Rappaport, S. 1994, *ApJ*, 437, 733
- Di Stefano, R., & Nelson, L. A. 1996, in *Supersoft X-Ray Sources*, ed. J. Greiner (Berlin:Springer), 3
- Ebisawa, K., et al. 2001, *ApJ*, 550, 1007
- Finoguenov, A., Jones, C., & Kudritzki, R. P. 2001, preprint
- Freedman, W. L., et al. 1994, *ApJ*, 427, 628
- Greiner, J. 1996, in *Supersoft X-Ray Sources*, ed. J. Greiner (Berlin:Springer), 299
- Greiner, J. 2000a, *New Astronomy*, 5, 137
- Greiner, J. 2000b, *New Astronomy Reviews*, 44, 149
- Hachisu, I., Kato, M., & Nomoto, K. 1996, *ApJ*, 470, L97
- Heise, J., van Teeseling, A., & Kahabka, P. 1994, *A&A*, 288, L45
- Hill, J. K., et al. 1992, *ApJ*, 395, L37
- Hughes, J. P. 1994, *ApJ*, 427, L25
- Iben, I. Jr 1982, *ApJ*, 259, 244
- Iben, I. Jr, & Livio, M. 1993, *PASP*, 105, 1373
- Iben, I. Jr, & Tutukov, A. V. 1985, *ApJS*, 58, 661
- Iben, I. Jr, & Tutukov, A. V. 1989, *ApJ*, 342, 430
- Iben, I. Jr, & Tutukov, A. V. 1994, *ApJ*, 431, 264
- Immler, S., & Wang, Q. D. 2001, *ApJ*, 554, 202
- Jacoby, G. H., Ciardullo, R., Ford, H. C., & Booth, J. 1989, *ApJ*, 344, 704
- Jordan, S., Schmutz, W., Wolff, B., Werner, K., & Mürset, U. 1996, *A&A*, 312, 897
- José, J., Hernanz, M., & Isern, J. 1993, *A&A*, 269, 291
- Kaaret, P. et al. 2001, *MNRAS*, 321, L29
- Kahabka, P. 1999, *A&A*, 344, 459
- Kahabka, P., Hartmann, H. W., Parmar, A. N., & Negueruela, I. 1999, *A&A*, 347, L43
- Kahabka, P., Parmar, A. N., & Hartmann, H. W. 1999, *A&A*, 346, 453
- Kahabka, P., & van den Heuvel, E. P. J. 1997, *ARA&A*, 35, 69
- Kato, M., & Hachisu, I. 1994, *ApJ*, 437, 802
- Kato, M. 1997, *ApJS*, 113, 121
- Kaufman, M., Bash, F. N., Hine, B., Rots, A. H., Elmegreen, D. M., & Hodge, P. W. 1989, *ApJ*, 345, 674
- Kaufman, M., Bash, F. N., Crane, P. C., & Jacoby, G. H. 1996, *AJ*, 112, 1021
- Kong, X., et al. 2000, *AJ*, 119, 2745
- Lewin, W. H. G., Van Paradijs, J., & Taam, R. E. 1995, in *X-ray Binaries*, ed. W. H. G. Lewin, J. van Paradijs, & E. P. J. van den Heuvel (Cambridge University Press, Cambridge) 175
- Livio, M. 1992, *ApJ*, 393, 516
- Magrini, L., Perinotto, M., Corradi, R. L. M., & Mampaso, A. 2001, *A&A*, 379, 90
- Makishima, K., et al. 1986, *ApJ*, 308, 635
- Makishima, K., et al. 2000, *ApJ*, 535, 632
- Matsumoto, H. et al. 2001, *ApJ*, 547, L25
- Matonick, D. M., & Fesen, R. A. 1997, *ApJS*, 112, 49
- Mihalas, D. 1978 *Stellar Atmospheres*, (Freeman:San Francisco)
- Motch, C., Hasinger, G., & Pietsch, W. 1994, *A&A* 284, 827
- Mukai, K. 1993, *Legacy*, 3, 21
- Mitsuda, K., et al. 1984, *PASJ*, 36, 741
- Paczynski, B. 1971, *Acta Astron.*, 21, 417
- Paerels, F., et al. 2001, *A&A*, 365, 308
- Parmar, A. N., et al. 1997, *A&A*, 323, L33
- Parmar, A. N., Kahabka, P., Hartmann, H. W., Heise, J., & Taylor, B. G. 1998, *A&A*, 332, 199
- Pence, W. D., Snowden, S. L., Mukai, K., & Kuntz, K. D. 2001, *ApJ*, 561, 189
- Rappaport, S., Chiang, E., Kallman, T., & Malina, R. 1994, *ApJ* 431, 237
- Rappaport, S., Di Stefano, R., & Smith, J. D. 1994, *ApJ* 426, 692
- Reichen, M., Kaufman, M., Blecha, A., Golay, M., & Huguenin, D. 1994, *A&AS*, 106, 523
- Remillard, R. A., Rappaport, S., & Macri, L. M. 1995, *ApJ* 439, 646
- Sarazin, C. L., Irwin, J. A., & Bregman, J. N. 2000, *ApJ*, 544, L101
- Sarazin, C. L., Irwin, J. A., & Bregman, J. N. 2001, *ApJ*, 556, 533
- Schaeidt, S., Hasinger, G., & Trümper, J. 1993, *A&A*, 270, L9
- Shakura, N. I., & Sunyaev, R. A. 1973, *A&A*, 24, 337
- Sion, E. M., & Starrfield, S. G. 1994, *ApJ*, 421, 261
- Southwell, K. A., Livio, M., Charles, P. A., O'Donoghue, D., & Sutherland, W. J. 1996, *ApJ*, 470, 1065
- Supper, R., et al. 1997, *A&A*, 317, 328
- Tennant, A. F., Wu, K., Ghosh, K. K., Kolodziejczak, J. J., & Swartz, D. A. 2001, *ApJ*, 549, L43
- Thomasson, M., & Donner, K. J. 1993, *A&A*, 272, 153
- Townsley, L. K., Broos, P. S., Garmire, G. P., & Nousek, J. A. 2000, *ApJ*, 534, L139
- Verbunt, F. & van den Heuvel, E. P. J. 1995, in *X-ray Binaries*, ed. W. H. G. Lewin, J. van Paradijs, & E. P. J. van den Heuvel (Cambridge University Press, Cambridge) 457
- Verner, D. A., Yakovlev, D. G., Band, I. M., Trzhaskovskaya, M. B. 1993, *AD&NDT*, 55, 233
- Verner, D. A., Yakovlev, D. G., 1995, *A&AS*, 109, 125
- van den Heuvel, E. P. J., Bhattacharya, D., Nomoto, K., & Rappaport, S. A. 1992, *A&A*, 262, 97
- Wand, Q. 1991, *MNRAS*, 252, 47p
- White, N. E., Giommi, P., Heise, J., Angelini, L., & Fantasia, S. 1995, *ApJ*, 445, L125
- Yungelson, L., Livio, M., Truran, J. W., Tutukov, A., & Fedorova, A. 1996, *ApJ*, 446, 890